## RESEARCH ARTICLE

**Key Points:**
- Foliation and foliation-parallel fractures oriented 60°/145° to 818 m depth suggest a similar Alpine Fault plane orientation at ~1 km depth
- Joints subvertical striking NW-SE above ~500 m and gently dipping below interpreted as exhumation-related and inherited hydrofractures
- The three fracture sets and subsidiary faults define an anisotropic permeability tensor enhanced by laterally varying topographic stresses

**Supporting Information:**
- Supporting Information S1
- Data Set S1

**Correspondence to:**
C. Massiot,
c.massiot@gns.cri.nz

# The Alpine Fault Hangingwall Viewed From Within: Structural Analysis of Ultrasonic Image Logs in the DFDP-2B Borehole, New Zealand

Cécile Massiot[1,2] , Bernard Célérier[3], Mai-Linh Doan[4] , Tim A. Little[2], John Townend[2] , David D. McNamara[5], Jack Williams[6,7] , Douglas R. Schmitt[8], Virginia G. Toy[6] , Rupert Sutherland[2] , Lucie Janku-Capova[2] , Phaedra Upton[1] , and Philippe A. Pezard[3]

[1]GNS Science, Avalon, Lower Hutt, New Zealand, [2]SGEES, Victoria University of Wellington, Wellington, New Zealand, [3]Géosciences Montpellier, Université de Montpellier, CNRS, Montpellier, France, [4]Univ. Grenoble Alpes, Univ. Savoie Mont Blanc, CNRS, IRD, IFSTTAR, ISTerre, Grenoble, France, [5]School of Natural Sciences, University of Ireland, Galway, Ireland, [6]Department of Geology, University of Otago, Dunedin, New Zealand, [7]School of Earth and Ocean Sciences, Cardiff University, Cardiff, UK, [8]Department of Physics, University of Alberta, Edmonton, AB, Canada

**Abstract** Ultrasonic image logs acquired in the DFDP-2B borehole yield the first continuous, subsurface description of the transition from schist to mylonite in the hangingwall of the Alpine Fault, New Zealand, to a depth of 818 m below surface. Three feature sets are delineated. One set, comprising foliation and foliation-parallel veins and fractures, has a constant orientation. The average dip direction of 145° is subparallel to the dip direction of the Alpine Fault, and the average dip magnitude of 60° is similar to nearby outcrop observations of foliation in the Alpine mylonites that occur immediately above the Alpine Fault. We suggest that this foliation orientation is similar to the Alpine Fault plane at ~1 km depth in the Whataroa valley. The other two auxiliary feature sets are interpreted as joints based on their morphology and orientation. Subvertical joints with NW-SE (137°) strike occurring dominantly above ~500 m are interpreted as being formed during the exhumation and unloading of the Alpine Fault's hangingwall. Gently dipping joints, predominantly observed below ~500 m, are interpreted as inherited hydrofractures exhumed from their depth of formation. These three fracture sets, combined with subsidiary brecciated fault zones, define the fluid pathways and anisotropic permeability directions. In addition, high topographic relief, which perturbs the stress tensor, likely enhances the slip potential and thus permeability of subvertical fractures below the ridges, and of gently dipping fractures below the valleys. Thus, DFDP-2B borehole observations support the inference of a large zone of enhanced permeability in the hangingwall of the Alpine Fault.

**Plain Language Summary** Fluids circulating near faults affect the occurrence of earthquakes. Near the Alpine Fault, South Island of New Zealand, fluids circulate through fractures. For the first time, measurements made in the DFDP-2B borehole reveal the nature and orientation of >2200 fractures and other features along a transect approaching the Alpine Fault to a depth of 818m below surface. Based on these measurements, we propose an orientation of the Alpine Fault at ~1km below surface in the Whataroa Valley, which to date has not been precisely imaged from other surveys. We observe three fracture sets: one present all along the borehole and parallel to the inferred Alpine Fault orientation; and two others whose proportions switch with depth, reflecting deep fracturing under high fluid pressures and unloading while the rock mass was brought up to surface. Together with additional subsidiary fault zone, these three fracture set orientations define the main directions of fluid circulations near the Alpine Fault in the Whataroa Valley. In addition, high topographic relief encountered near the Alpine Fault likely enhances permeability of vertical fractures under the ridges, and horizontal fractures below the valleys.

## 1. Introduction

Fault rocks record cumulative effects made by a range of processes in successive deformation events on the main fault plane and eventual subsidiary faults (Caine et al., 1996; Chester et al., 1993; Faulkner et al., 2010; Lin et al., 2007). Direct subsurface measurements of structural, petrophysical, and hydrological properties near the Alpine Fault, the major plate boundary between the Pacific and Australian plates in the South Island of New

Zealand, have previously been limited to shallow tunnels (Cox et al., 2015) and boreholes (Sutherland et al., 2012). These shallow observations may not represent conditions at greater depth due to surface processes associated with stress release, weathering, or the impacts of topography (Sutherland et al., 2017; Upton et al., 2018). Drilling in the vicinity of active faults remains the only way to evaluate the in situ conditions at which earthquakes are generated and damage zones develop (Zoback et al., 2007). The DFDP-2B borehole was drilled in the hangingwall of the Alpine Fault in 2014 to a true vertical depth of 818 m beneath the Whataroa valley, central Southern Alps (Figure 1) as part of the Deep Fault Drilling Project (DFDP), to study the state of the crust near the Alpine Fault and better understand fault zone processes (Townend et al., 2009).

The interpretation of image logs in active fault zones has revealed important information about the structure, stress state, and permeability at depth (Barton et al., 1995; Brudy & Zoback, 1999; Conin et al., 2014;
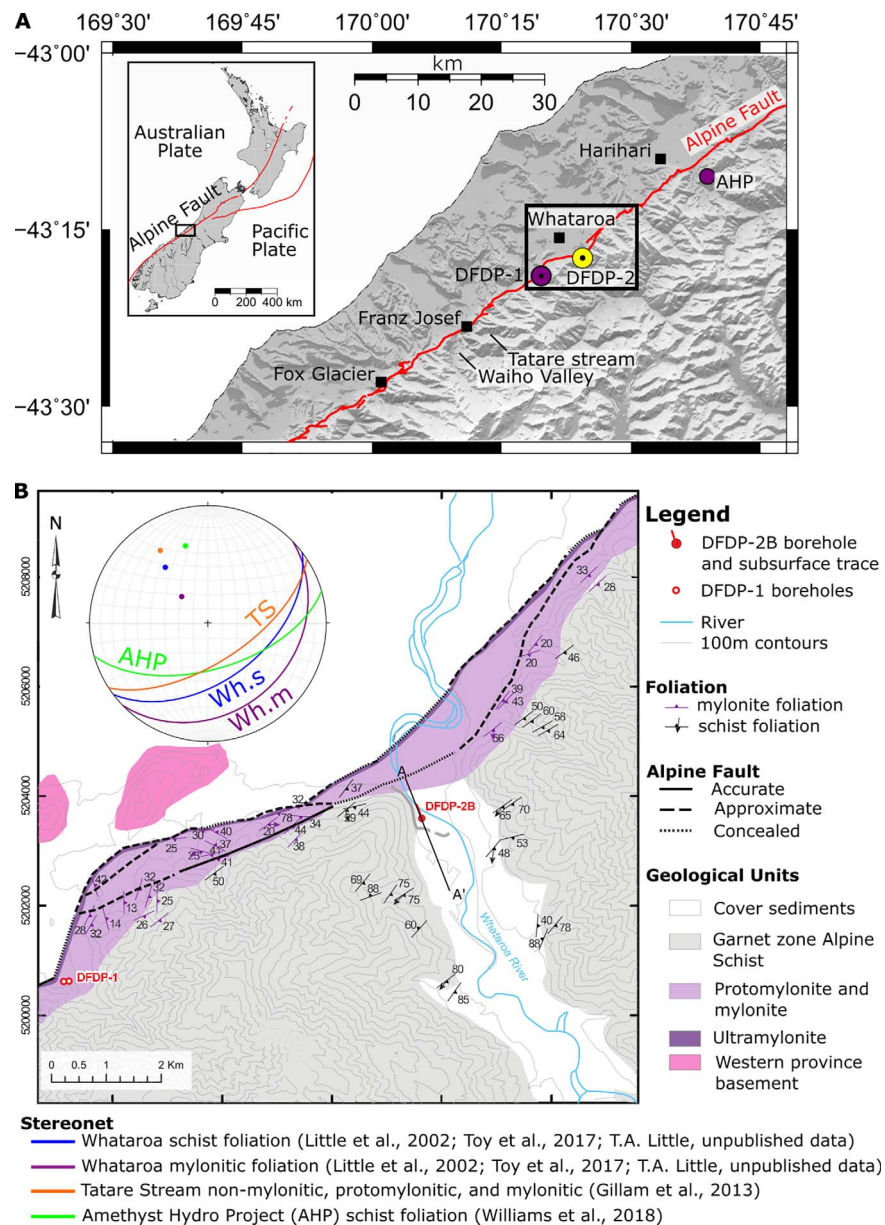


**Figure 1.** Regional settings and summary of foliation orientations in nearby areas. (a) Shaded digital elevation model with DFDP-2 and DFDP-1 boreholes, Alpine Fault, and nearby townships locations. The inset shows the map location in New Zealand, and plate boundaries as red lines. (b) Geological map and mean foliation orientations in and near the Whataroa Valley (after Gillam et al., 2013; Little et al., 2002; T. A. Little, Personal Communication, 2018; Toy et al., 2017; Williams et al., 2018). A-A′: cross section shown in Figure 2.

Daniel et al., 2004; Hickman & Zoback, 2004; Pezard & Luthi, 1988), that control the behavior of fault zones (e.g., Faulkner et al., 2010; Townend et al., 2009). In recent years, several rapid response drilling projects were carried out near active faults directly after large earthquakes to understand the postearthquake state of a fault (Ito & Kiguchi, 2005; Nojima Fault, 1995 Kobe earthquake; Hung et al., 2009; Chelungpu Fault, 1999 Chi-chi earthquake; Lin et al., 2013; 2011 Tohoku-Oki earthquake; Nie et al., 2013; 2008 Wenchuan earthquake). In contrast, relatively few observations have been made on faults that are late in their interseismic cycle. The Alpine Fault fails in large or great earthquakes every 291 ± 23 years and last ruptured in AD 1717 (Berryman et al., 2012; Cochran et al., 2017; Sutherland et al., 2007). We present interpretations of the image logs acquired in the DFDP-2B borehole, which provide new information about conditions in the hangingwall of a plate boundary fault in its preearthquake state.

A series of borehole geophysical logs was acquired in DFDP-2B between 264 and 893 m (measured along the deviated borehole) in metamorphosed schists (Sutherland et al., 2015, 2017; Townend et al., 2017; Toy et al., 2017). Downhole geophysical logs record petrophysical parameters continuously along the borehole (e.g., Rider, 1996), providing an intermediate scale of observation between laboratory and seismic experiments (Boness & Zoback, 2006; Jeppson & Tobin, 2015; Schijns et al., 2012). Ultrasonic images of the borehole surface, commonly called borehole TeleViewer (BHTV) logs, provide images of the borehole wall surface oriented with respect to north, by measuring the travel time and impedance of ultrasonic pulses sent and received by a piezoelectric transducer (Poppelreiter et al., 2010; Zemanek et al., 1970). BHTV log interpretation allows the detection of fabrics and structures intersecting the borehole (bedding, foliation, fractures, veins, etc.) together with their orientation and morphological characteristics; stress-induced features when present; and of the relative ultrasonic reflectivity of the rock at the borehole wall. With only 1.4 m of nonoriented core recovered in DFDP-2B (Sutherland et al., 2015; Toy et al., 2017), the interpretation of the BHTV logs offer the best opportunity to interpret the nature of the geological structures (e.g., foliation planes and fractures) intersecting the borehole and to measure their orientations.

The metamorphic rock types that compose the variably mylonitized hangingwall of the Alpine Fault have so far been rarely described using image logs (see Barton & Zoback, 2002; Burns, 1987). Some coarse-grained gneissic lithologies have been studied (e.g., Wenning et al., 2017), but have largely been based on resistivity image logs, or on drill core descriptions (Barton & Zoback, 2002; Blake & Davatzes, 2012; Paillet & Kapucu, 1989; Williams & Johnson, 2004). For the Alpine Fault data described here, we therefore devised a specific BHTV log analysis method, based on a descriptive classification and integration with outcrop studies. The preliminary results presented in Townend et al. (2017) are thus herein largely expanded.

In this paper, we measure and interpret the foliation and other structures in the hangingwall schists of the Alpine Fault using the high-resolution BHTV logs acquired in the DFDP-2B borehole. It is the first description of a continuous sequence where the intensity of deformation (mylonitization) increases as the Alpine Fault is approached. The flow of groundwater through these fracture systems results in large variations in temperature and fluid pressure adjacent to the Alpine Fault, that, in turn, affect rock deformation processes, slip and mineralization on geological faults, and hence the distribution of earthquakes (Sutherland et al., 2017). Our results, therefore, are significant for understanding the evolution of fracture systems adjacent to active faults, and hence for understanding earthquake processes. First, we present the geological settings of the DFDP-2B borehole. Second, we detail the BHTV logs acquisition, processing, and analysis methods. Third, we present the results of the analysis of planar features (foliation planes and natural fractures), and the delineation of ultrasonic image facies. Finally, we interpret these ultrasonic image facies and planar features in the context of structures observed in existing nearby exposures of the Alpine Fault's hangingwall, and discuss the implications for permeability in this fractured rock mass under a range of possible stresses.

### 1.1. Geological Setting

The Alpine Fault is a ~850 km long dextral transpressive fault which forms part of the plate boundary between the Pacific and Australian plates in the South Island of New Zealand (Sibson et al., 1979; 1981). The central Southern Alps section of the Alpine Fault has an average strike of ~055° (i.e., a dip direction of 145°) and dip of 45°SE–60°SE to depths of ~15 km depth (see e.g., Feenstra et al., 2016; Gillam et al., 2013; Norris & Cooper, 2007; Sibson et al., 1981; Stern et al., 2007). In the shallow subsurface, the Alpine Fault is segmented into a series of oblique-reverse (SE-dipping) and strike-slip (vertical) sections (Norris & Cooper, 2007).

Rapid exhumation along the fault plane brings to the surface rocks that experienced midcrustal conditions only 1–2 Myr ago (Little et al., 2005; Norris et al., 1990). The up to ~1 km thick sequence of rocks that formed within the ductile shear zone of the Alpine Fault at mid to lower crustal depth comprises protomylonites, mylonites, and ultramylonites. These variably ductilely deformed rocks were derived from a protolith of Torlesse Composite Terrane-derived Alpine Schists that are garnet grade (amphibolite facies) in the hangingwall immediately to the east of the Alpine Fault. Inside the Alpine mylonite zone, the rocks have accommodated an increasing intensity of Neogene finite shear strain with proximity to the principal slip zone of the Alpine Fault (Norris & Cooper, 2007; Toy et al., 2012, 2017). The Alpine Schists are S > L tectonites, with strong planar foliations defined by millimeter-spaced to centimeter-spaced quartz-feldspar and mica segregations. In the Alpine Schist outside of the mylonite zone, the mostly steeply dipping nonmylonitic foliation is commonly defined by crenulations (microfolds) of older fabrics, the hinges of which define a strong quartz rodding (intersection) lineation (Little et al., 2002; Norris et al., 2007; Toy et al., 2012). The Neogene mylonitization has resulted in an intensification and transposition of the older schist foliation. Ductilely deformed quartzo-feldspathic vein segregations subparallel to the mylonitic foliation are common, whereas discordant veins are rare. The Neogene shearing overprint also introduced new, obliquely cross cutting, millimeter-to-centimeter-spaced, extensional shear bands, particularly in protomylonites, that cut and offset the local foliation. Closest to the Alpine Fault, the highest-strain ultramylonitic rocks may have relatively weakly expressed foliation due to pervasive grain-scale mixing of the very fine-grained constituent minerals (Toy et al., 2012).

Foliations measured in two well-exposed outcrops of protomylonite and mylonite 30 km south of the Whataroa Valley along-strike of the Alpine Fault (Figure 1) yield average orientations of 63°/143° at Tatare Stream (Gillam et al., 2013), and 34°/129° at Stony Creek (Little et al., 2016). In the Whataroa Valley, scarce exposures reveal a similar mylonitic and nonmylonitic foliation orientation (Little et al., 2002; Toy et al., 2017; and T. A. Little, unpublished data). In Alpine Schist drill-cores of the Amethyst Hydro Project ~20 km north of the Whataroa Valley, and ~0.7–2.0 km measured orthogonally from the principal slip zone of the Alpine Fault, nonmylonitic foliation and foliation-parallel fractures have an average orientation of 58°/164° (Williams et al., 2018). In outcrop, foliations in the Alpine mylonites typically dip SE at ~25–65° in at least approximate parallelism with the Alpine Fault—a pattern that is complicated by the strong segmentation of that fault in the near surface (Gillam et al., 2013; Little et al., 2002; Toy et al., 2012). In outcrops of the Alpine Schist and the Alpine mylonite zone, joints are commonly disposed in approximate orthogonality to the local foliation, and are at least in part related to the exhumation of the hangingwall (e.g., Gillam et al., 2013; Hanson et al., 1990; Holm et al., 1989; Little et al., 2002; Toy et al., 2012).

Focal mechanism inversion of present-day seismicity (to depths of 8–10 km) yields a maximum horizontal compressive stress direction $\sigma_1$ of $115 \pm 10°$ and predominantly strike-slip stress regime, hence with a subvertical intermediate principal stress direction ($\sigma_2$; Boese et al., 2012). Geological studies suggest that the intermediate and minimum principal paleostresses ($\sigma_2$ and $\sigma_3$) may be close in magnitude. In Alpine Schists exhumed from midcrustal depths near Franz Josef Glacier, Holm et al. (1989) documented open, gently dipping, extension cracks, and also mineralized veins (hydrofractures), that they inferred to record a fluid overpressured paleostress state associated with a vertical $\sigma_3$ direction. Analysis of extensional shear bands in the Alpine mylonites revealed that the closeness in magnitude of $\sigma_2$ and $\sigma_3$ allowed the flipping between the two stress principal directions, presumably at a depth just below the brittle-ductile transition.

### 1.2. Deep Fault Drilling Project (DFDP)

The two boreholes drilled during the first phase of the DFDP programme at Gaunt Creek (DFDP-1A, 100 m depth; DFDP-1B, 152 m depth) sampled shallow fault rocks in the central Alpine Fault (Figure 1; Sutherland et al., 2012). Lithological (Schleicher et al., 2015; Toy et al., 2015), structural (Williams et al., 2016, 2017), physical (Boulton et al., 2012; Ikari et al., 2014, 2015), and hydraulic (Carpenter et al., 2014) properties were obtained from drill-cores, while wireline logging analysis and hydraulic measurements provided details of the structure and petrophysical properties of a geochemically distinct alteration zone (Sutherland et al., 2012; Townend et al., 2013). BHTV log interpretation in DFDP-1B indicates that centimeter-thick-scale features with orientations similar to that of the Alpine Fault (dip magnitude and direction of 43°/105°) predominate throughout the logged interval, with a subordinate set of north-dipping features (Townend et al., 2013).
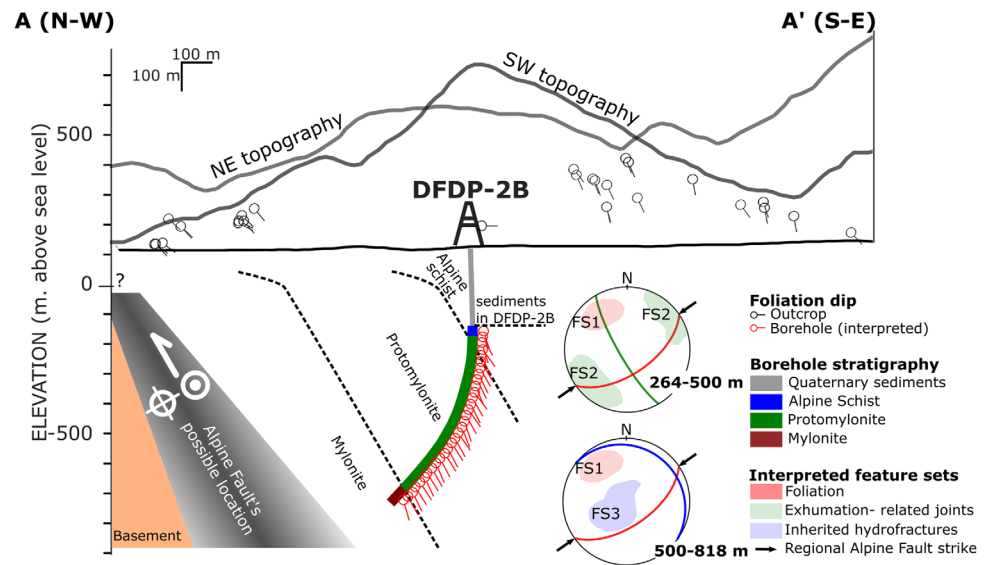
**Figure 2.** Schematic cross section along the Whataroa Valley (line A-A' in Figure 1) of foliation orientations measured in outcrop and interpreted in DFDP-2B; and summary lower-hemisphere stereogram of the three main feature sets (density contours of poles to planar structures and great circles of mean orientations). The possible locations of the Alpine Fault are shaded in gray, assuming a 50–70° dip; the location at surface, near-surface geometry and location at depth of the Alpine Fault and limits between mylonite, protomylonite and Alpine schist are not well constrained.

The second phase of DFDP ("DFDP-2") was designed to intersect the Alpine Fault at ∼1 km depth so that topographic effects on stress are diminished (Upton et al., 2018). DFDP-2B was drilled in 2014 in the Whataroa Valley to a depth of 893 m measured drillers' depth along the borehole (corresponding to 818 m vertical depth), but did not reach its target due to technical difficulties (Sutherland et al., 2015; all depths reported in this paper are reported according to drillers' depth along the borehole; Figures 1 and 2). The borehole trajectory was determined from integration of the continuously logged magnetic field orientations and instrument inclination from the BHTV logging tool itself. The borehole deviates from vertical steadily with depth from the ground surface to reach a stable inclination of ∼44° and an azimuth of ∼340°. Cuttings and wireline logs, run between the bottom of the casing set in the basement rocks (264 m) and the bottom depth (893 m), sampled the hangingwall of the Alpine Fault in detail (Sutherland et al., 2017; Townend et al., 2017; Toy et al., 2017). The stratigraphy defined from cuttings analysis comprises Quaternary sedimentary formations from the surface to 239 m, then a succession of rocks that have accommodated an increasing creep shear strain with depth: namely Alpine Schist to 280 m, protomylonites to 852 m and mylonites to 893 m (Figure 2, Toy et al., 2017). Cuttings cannot reveal <1 m lithological variations because they are sampled only every 2 m and subject to mixing during their trip up the borehole. A total of 19.14 km of wireline logs were acquired during 18 sessions in the 264–889 m section of DFDP-2B, including 4.8 km of BHTV logs acquired during successive sessions (Sutherland et al., 2015; Townend et al., 2017). From 1 to 13 months after the end of drilling operations (latest measurement to date), a major change in equilibrium temperature gradient was measured at ∼730 m via a distributed temperature sensing optical fiber installed behind the casing (Sutherland et al., 2017). Extensive passive and active seismic measurements using both this fiber optical cable and downhole geophone sensors also followed in order to better delineate the fault (Constantinou et al., 2016; Hall et al., 2017).

## 2. Borehole Televiewer (BHTV) Log Processing and Analysis Methods

### 2.1. BHTV Logging and Processing

BHTV tools emit and receive high frequency, ultrasonic pulses (generally between 500 kHz and 2 MHz) generated by an ultrasonic transducer. This transducer is either positioned in a 360° rotating head, or fixed along the downhole tool axis, emitting pulses in the direction of a 45° inclined rotating mirror located

below the transducer, as in the case of the ABI® tool from ALT used in DFDP-2. The processing of the ultrasonic pulses reflected from the borehole surface generate two oriented maps of the inside surface of the borehole, one with travel time and the other with the reflected pulse amplitude (Poppelreiter et al., 2010; Zemanek et al., 1970). The pulse's two-way travel time measures the distance between the borehole wall and the tool, and hence estimates the borehole's shape and diameter. The ultrasonic wave amplitude depends on relative variations in the ultrasonic impedance and roughness of the borehole wall, which thus varies with mineralogy, texture, and fracturing (e.g., Davatzes & Hickman, 2010). Log acquisition and processing are described in Appendix A. All BHTV images and interpreted feature orientations presented in this paper are with reference to geographic north from triaxial flux-gate magnetometers contained within the tool. The borehole deviation has been taken into account during dip magnitude and dip direction computations.

An estimation of the borehole diameter ("caliper") is required for the calculation of the orientation of planar features detected in BHTV logs (Zemanek et al., 1970) and for the interpretation of other well logs (in particular the resistivity logs; Remaud, 2015). Discrete increases in borehole diameter are good indicators of individual fractures or fractured zones, while larger-scale variations can indicate larger fractured zones or changes between harder and softer rocks (e.g., Massiot et al., 2015). Regretfully, a three-arm mechanical caliper ran in DFDP-2B did not provide reliable measurements due to borehole inclination and the tool collapsing under its own weight. The procedures used to estimate the borehole diameter from the BHTV travel time, taking into account the variable speed of sound in the drilling mud, is presented in Appendix B.

## 2.2. BHTV Log Quality
The BHTV logs were of variable quality due to mud attenuation, and drilling and logging tool effects (see supporting information; Lofts & Bourke, 1999). Identifying image artifacts and their causes is a critical step in the analysis of ultrasonic image facies, as well as of feature orientation and density variations with depth. The ability to delineate planar features is diminished in areas where BHTV images do not cover the full circumference, and this study is based on a compilation of the best quality logs for the 264–888 m interval (Appendix A).

Image quality is ranked within three levels primarily defined by borehole azimuthal coverage: bad, poor, and good image quality correspond to <25%, 25–50%, and >50% coverage respectively. The presence of artifacts further decreases the quality ranking in places. Overall, the image quality is good with small intervals of bad quality in the 260–558 m interval (Figure 3). In the 558–598 m interval, image quality is bad with only small portions of the borehole observable. The 598–893 m interval is characterized by intercalation of thin (<1 m) zones of bad to poor quality within otherwise zones of good image quality (Figure 3). These thin intervals of poorer quality likely reflect spalling from the borehole wall either due to drilling or the presence of intensely fractured zones. Particular attention will be given to the 476–545 m interval where the image quality is best.

## 2.3. Characterization of Planar Features
Planar features that have a contrast in ultrasonic impedance—and in cases travel time—with the surrounding formation appear as a sinusoid on unwrapped BHTV logs (Zemanek et al., 1970). The BHTV log alone cannot differentiate between open or closed fractures (used here in a general term, i.e., including faults), veins, and mineral segregations forming part of the foliation (mica and quartz-rich layers). Thus, we use a descriptive classification system of the planar features in terms of contrast, morphology, planarity, and thickness (Figure 4).

The contrast of ultrasonic amplitude of planar features with respect to background observed on the amplitude images classifies feature appearance into three types: A, B, and C (Table 1 and Figure 4). Type A features are strongly contrasting. When of low ultrasonic amplitude, they are labeled A-L, or A-LT in the case where they are also visible on the travel time image and commonly associated with signal loss. Schmitt (1993) interpreted A-LT fractures as open in a granitic pluton, but Massiot et al. (2017) showed that this is not always the case in hydrothermally altered volcanic rocks. When of high amplitude, they were never seen on the travel time image, and are labeled A–H. Types B and C are moderately and weakly contrasted,
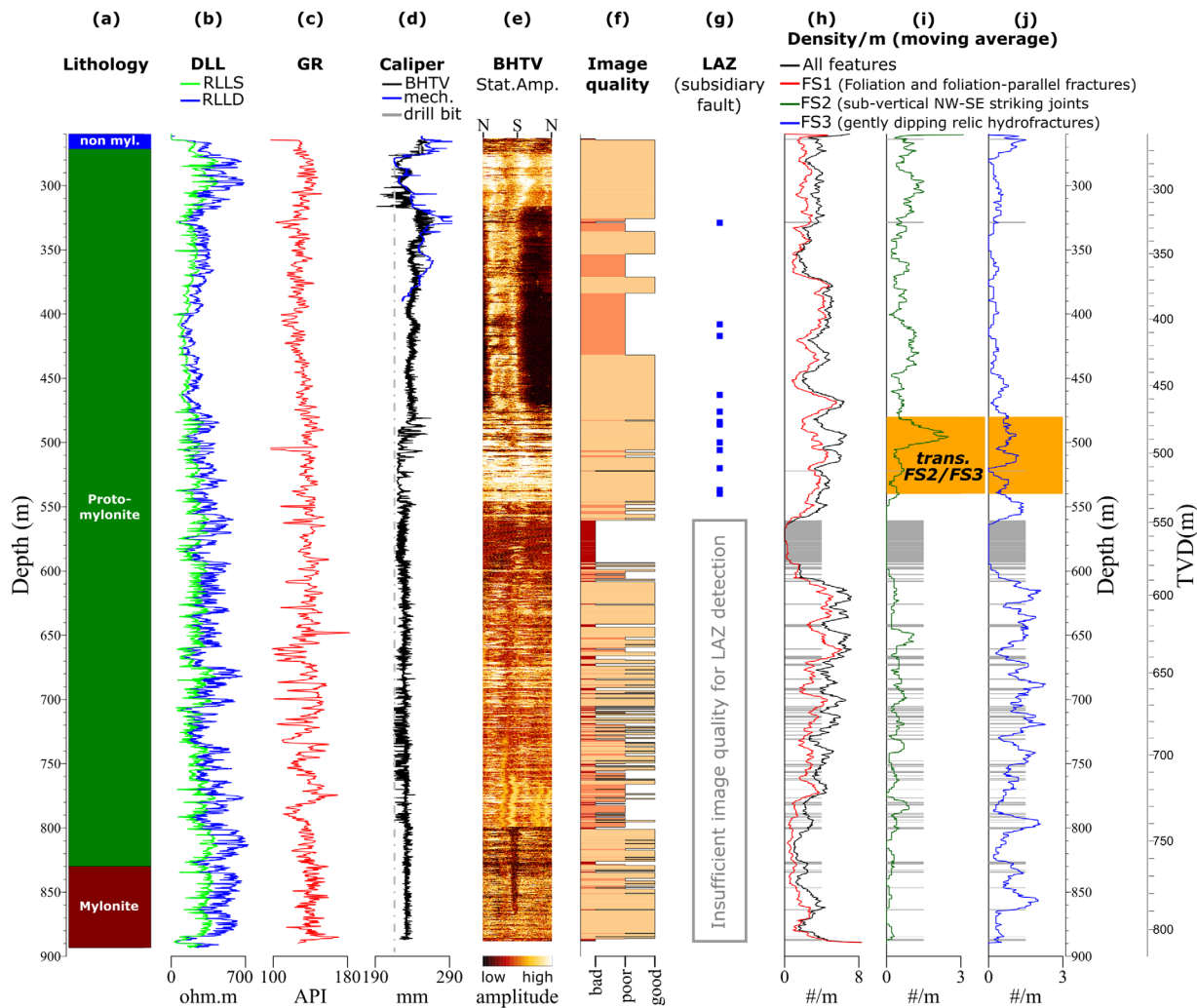
**Figure 3.** Composite of BHTV log interpretation and other wireline logs used in this study. From left to right: (a) lithology, (b) dual laterolog (shallow resistivity RLLS, deep resistivity RLLD), (c) natural gamma-ray, (d) caliper: mechanical, computed from BHTV travel time (Appendix B), and drill-bit size, (e) Statically normalized BHTV amplitude image, (f) BHTV log quality, (g) occurrence of low ultrasonic amplitude zones; (h–j) planar features density with a 10 m window moving average: for all features and FS1 features, (i) FS2, and (j) FS3. Note the different scale between (h) and (i and j). The 480–540 m transition zone between (h) FS2 and FS3 predominance is highlighted by an orange shaded rectangle. *Gray zones in Figures 3g–3i are of bad BHTV log quality.*

respectively. Type B and C features are sampled by a representative sinusoid every 10–30 cm where they belong to a series of subparallel features.

The morphology of each feature is described in terms of its continuity around the borehole in five categories (Table 2): continuous, discontinuous, partial, truncated, and obscured, the latter linked to poor image quality. Planarity is classified in two categories: planar and near-planar, according to how closely they fit a sinusoid. The apparent thickness of each type A feature is measured on the image and converted to the true thickness measured orthogonally to the feature (Barton & Zoback, 1992; Massiot et al., 2015). The thickness of type B and C features is too small to be evaluated. While the smallest observed apparent thickness is 2 mm (the BHTV log resolution), the conversion from apparent to feature-normal thickness reduces the thickness value, which can thus become lower than the BHTV log resolution.

The analysis of feature orientations is made on a weighted data set which compensates for the undersampling of features subparallel to the borehole (Massiot et al., 2015; Terzaghi, 1965; Yow, 1987). Because of the steadily increase in borehole deviation, the orientation of features subparallel to the borehole most affected by the undersampling varies with depth, as presented in Figure 5.
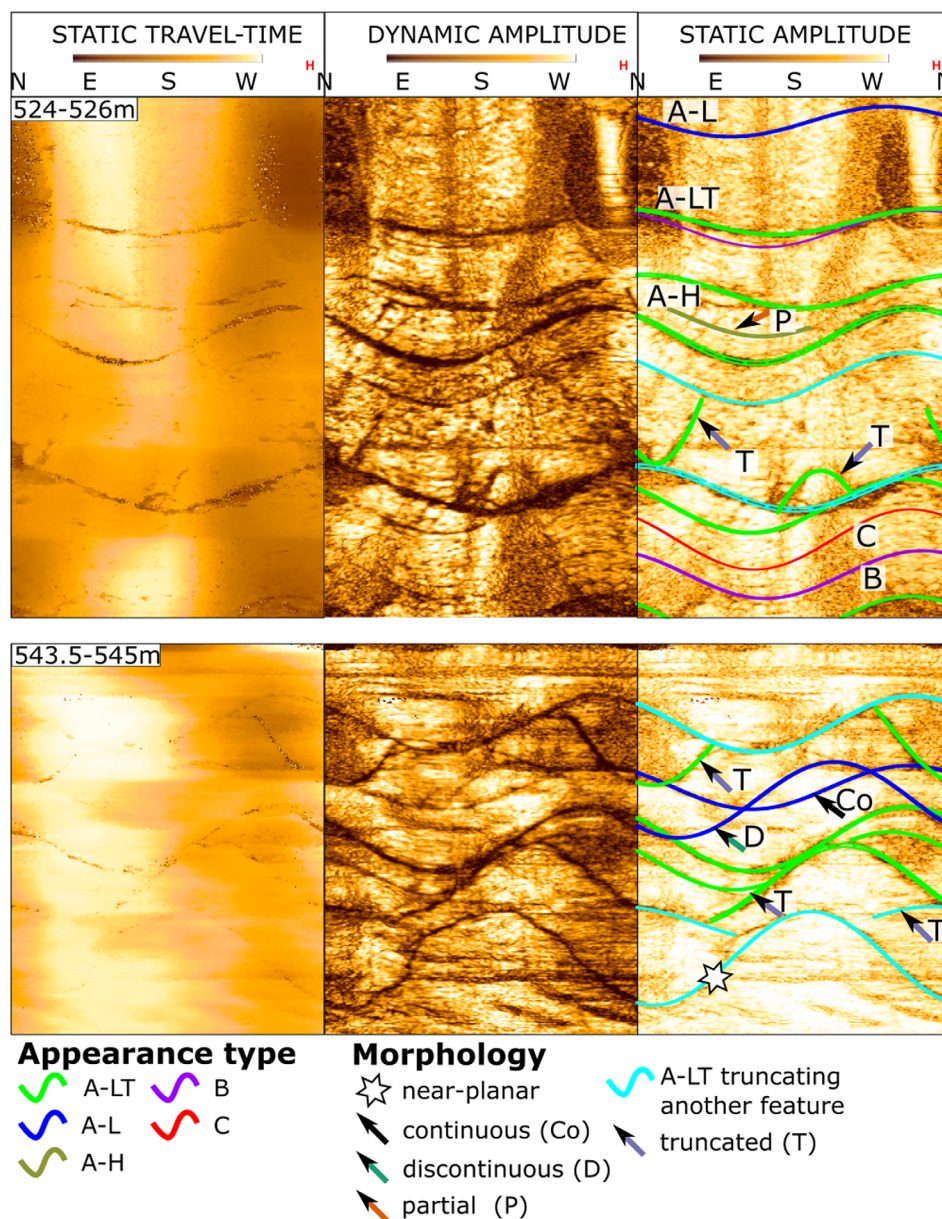
**Figure 4.** Feature morphology and descriptors. A-LT, A-L, A-H, B, and C refer to the appearance of features; Co, D, P, and T refer to morphological descriptors (see Tables 1 and 2 for more details). *Images are displayed unwrapped clockwise and oriented to geographic north.* H *indicates the high side of the borehole.*

**Table 1**
*Appearance of the Planar Features*

| Type | Amplitude contrast | Amplitude value | Seen on travel time image |
|------|-------------------|-----------------|---------------------------|
| A-LT | High | Low | Yes |
| A-L | High | Low | No |
| A-H | High | High | No |
| B | Moderate[a] | Low | No |
| C | Low[a] | Low | No |

[a]Part of a series of subparallel, closely spaced (1–3 cm) subplanar features.

No stress-induced borehole failures (as described by e.g., Massiot et al., 2015; Schmitt et al., 2012; Zoback et al., 2003) were observed in DFDP-2B BHTV logs with confidence.

### 2.4. Ultrasonic Image Facies Delineation

Variations in the gross appearance of BHTV logs can be observed on the statically normalized images. The combination of an ultrasonic amplitude range (low/high), overall appearance (grainy/smooth), and caliper from the travel time image, defines ultrasonic image facies. Drilling and logging artifacts account for a number of these variations (supporting information), and have been clearly isolated.

**Table 2**
*Morphology of the Planar Features*

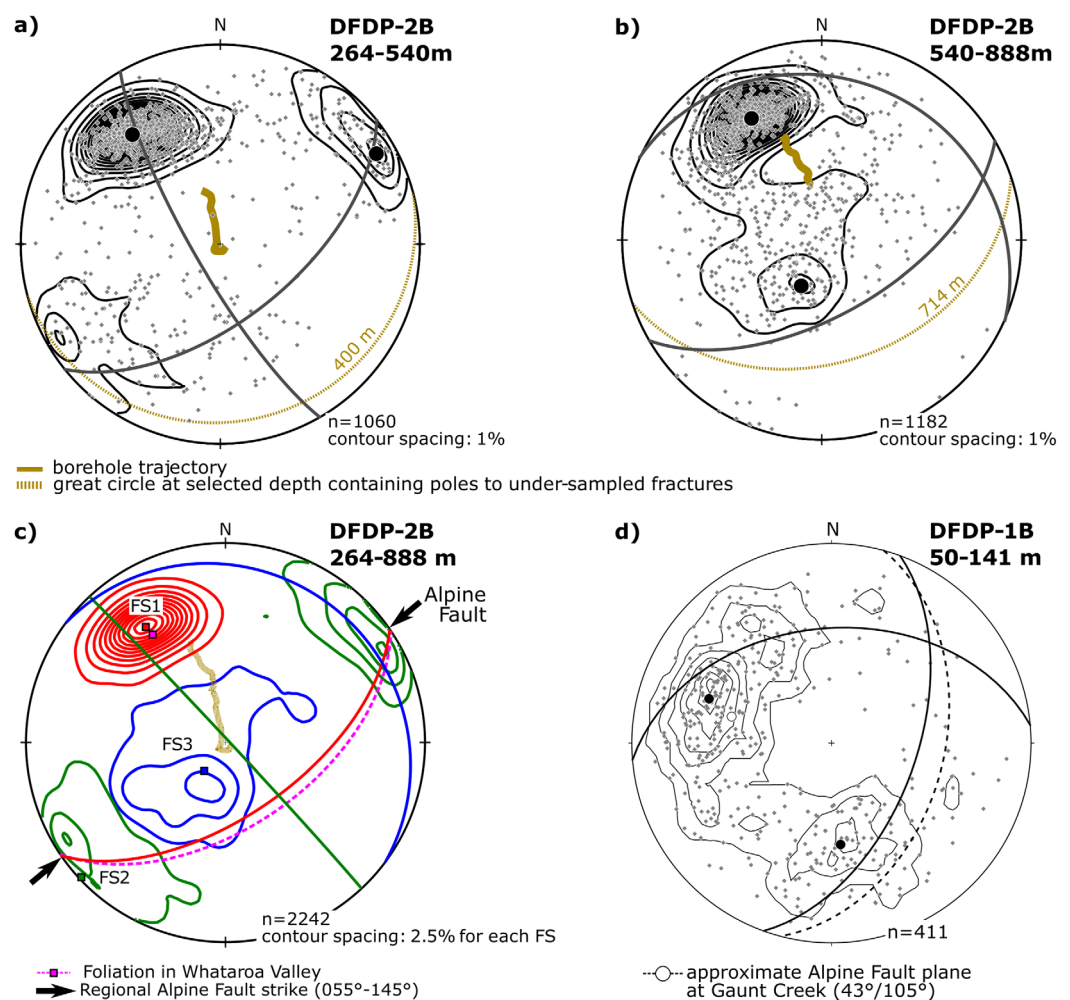| Continuity | Definition |
| --- | --- |
| Continuous (C) | Full sinusoid observed >270° around the borehole |
| Discontinuous (D) | Sinusoid observed in parts >270° cumulated around the borehole |
| Partial (P) | Partial sinusoid (i.e., observed 90–270° around the borehole) with at least one end observed |
| Truncated (T) | Partial sinusoid which stops on another feature |
| Obscured (O) | Partial sinusoid with both ends masked by bad image quality |



**Figure 5.** Lower-hemisphere, equal-area stereographic representations of features identified in the BHTV logs in DFDP-1B and DFDP-2B boreholes. (a) DFDP-2B, 264–540 m interval (number, *n* = 1060). (b) DFDP-2B, 540–888 m interval (*n* = 1182). (c) DFDP-2B: Fisher contours and mean orientation of poles to the three interpreted feature sets after being separated (*n* = 2242); mean foliation orientation in the Whataroa Valley; and regional strike of the Alpine Fault. (d) Feature orientation in the DFDP-1B borehole (after Townend et al., 2013) with the approximate Alpine Fault plane orientation at Gaunt Creek as a dashed great circle, white circle representing its pole. In Figures 5a–5b–5d, gray symbols are poles to features. Gray lines show Fisher contour intervals at 1% (Figures 5a–5b–5d) and 2.5% (Figure 5c) intervals. Large black circles mark the positions of the modal orientations, and solid great circles show the corresponding planes. Yellow dashed great circles in Figures 5a and 5b represent the poles planes of undersampled features parallel to the borehole at 400 and 714 m, respectively. The orientation of this great circle for each depth is the borehole trajectory (represented as yellow solid line).

## 3. Results

### 3.1. Planar Feature Orientation

The 2,242 planar features identified on the BHTV log have three dominant orientations, which we here refer to as feature sets (Figure 5 and Table 3). Feature set 1 (FS1), which contains two-thirds of the features, has a constant orientation over the entire logged interval, with a mean dip and dip direction of 60°/145° and is very clustered (resultant vector length of 0.97; Figure 5 and Table 3; Priest, 1993). This set comprises the foliation and will be discussed in section 4.1. The delineation of the two other feature sets is based primarily on their orientation and coincides with their occurrence either above or below ∼500 m depth (section 3.2 and Figure 5). Feature set 2 (FS2) contains NW-SE-striking features steeply dipping (>50°) to both SW and NE directions, with a 89°/047° mean orientation (Figure 5a). Feature set 3 (FS3) contains gently dipping (<50°) features of various dip direction, and a 15°/037° mean orientation (Figure 5b). FS2 and FS3 are less clustered than FS1 (resultant vector lengths of 0.84 and 0.87, respectively).

### 3.2. Planar Feature Density

The feature density is analyzed using a moving average (10 m window size; Figures 3g–3i). The calculations have been made on the raw dataset, so that linear fracture counts can be read off the graph. Feature densities calculated using the dataset corrected for the under-sampling of fractures subparallel to the borehole (not presented here for clarity) display the same trends. The BHTV log quality strongly influences the feature density: zones of bad quality have very few recognized features (see gray shaded zones in Figures 3g–3i). While poor log quality may hinder the detection of some features, most type A features are still detectable in these zones. The density analysis is reliable within zones of good image quality but is also made with caution in zones of poor image quality. Type B features are mainly located within the 490–550 m interval, a zone of good image quality where the ultrasonic impedance contrast is generally better than in other zones, and are considered to be geologically similar to type C features.

Overall, the feature density is 3.6 m$^{-1}$ average and up to 7.2 m$^{-1}$ at 620 and 660 m. Figure 3 highlights the transition zone between depths at which FS2 and FS3 predominate. While FS2 and FS3 features are present throughout the logged interval, FS2 is more frequent than FS3 in the 260–510 m interval, with a high-density peak at 480–500 m, and FS3 is more frequent than FS2 in the 520–888 m interval. The density profiles of the whole dataset and FS1 features alone are very similar, with an average density of 2.4 m$^{-1}$ (Figure 3g). FS1 feature density is low (0.3–1.6 m$^{-1}$) at 780–855 m.

### 3.3. Relationships Between Planar Feature Appearance, Morphology, and Orientation

Type A-LT features have the same distribution of orientations as the overall data set, which is expected as they represent 70% of the dataset (Table 3). The three type A-H features are of FS1 orientation, and of partial or obscured morphology. Other features of high ultrasonic amplitude are observed in various locations but are not reported because they span <25% of the borehole perimeter. Nearly all type B and C features are of FS1 orientation.

The majority of features are of continuous morphology (Table 3). Partial features are dominantly of FS2 orientation, with a few in the FS1 set. The truncated features are dominantly of FS2 and FS3 orientations and

**Table 3**

*Number and Orientation (Dip Magnitude/Dip Direction) of Planar Features for Each Feature Set (FS), Characterized by Their Appearance (Table 1), Morphology (Table 2) and Planarity (npl.: Near-Planar; pl.: Planar)*

| FS | Orientation | Appearance | | | | | Morphology | | | | | Planarity | | Total |
|---|---|---|---|---|---|---|---|---|---|---|---|---|---|---|
| | | A-LT | A-L | A-H | B | C | C | D | P | T | I | npl. | pl. | |
| FS1 | 60/145 | 972 | 151 | 3 | 98 | 294 | 932 | 185 | 15 | 16 | 370 | 5 | 1,513 | 1,518 |
| FS2 | 89/047 | 259 | 35 | 0 | 2 | 2 | 97 | 38 | 75 | 36 | 52 | 9 | 289 | 298 |
| FS3 | 15/037 | 332 | 83 | 0 | 7 | 4 | 273 | 91 | 11 | 15 | 36 | 5 | 421 | 426 |
| Total | | 1,563 | 269 | 3 | 107 | 300 | 1,302 | 314 | 101 | 67 | 458 | 19 | 2,223 | 2,242 |

terminate on features of FS1 orientation, although the contrary is also observed. The rare features with near-planar morphologies are found in all three fracture sets (Table 3).

The detection of near-planar, partial, and truncated features requires a good image quality. Poorer image quality below 545 m likely hinders their detection. It is thus possible that features of these morphologies and FS3 orientation below 545 m occur more frequently than what is detected on the BHTV log.

### 3.4. Planar Feature Thickness

After correcting for the intersection angle between fractures and borehole, the fracture-normal thickness of type A features ranges between 0.5 and 32 mm with a mean of 4.2 mm; only 10% of features have thickness >7 mm. Type A-LT features are thicker than type A-L's (mean thickness of 4.5 and 2.8 mm, respectively). The three type A-H features are relatively thick (3.2; 6.5 and 7 mm) compared to other feature types. There is no clear correlation between feature orientation and thickness. The 1% of features >15 mm occur throughout the logged interval, though are more numerous between 476–540 m and 812–852 m. The thickest feature is located at 520 m, belongs to FS1, and is associated with a slight caliper increase and zone of low ultrasonic amplitude (see section 3.5).

### 3.5. Low-Amplitude Zones and Ultrasonic Image Facies

Low ultrasonic amplitude zones that contain type A features, and where low ultrasonic amplitude is also observed between the type A features, occur in eleven locations between 260 and 545 m (Figures 3 and 6). Low ultrasonic amplitude zones are 0.5–3 m thick, have brecciated textures (with clasts being a few centimeter across), contain numerous type A features, and often coincide with low resistivity (deep and shallow), and caliper increases (Figure 6). Two configurations of these zones are observed: (1) pervasive low ultrasonic amplitudes associated with one or more FS1 features, and (2) low ultrasonic amplitudes confined between two FS1 features. The absence of low ultrasonic amplitude zones below 545 m is likely due to the poorer image quality preventing their observation, though some thin (0.5–3 m) zones of bad image quality may represent low ultrasonic amplitude zones (see section 4.4).

The 490–545 m interval is of particularly good image quality with few artifacts. Within this interval, three ultrasonic image facies (UAF) separated by gradational boundaries are recognized (Figure 6):

1. UAF1 has low caliper values (220–225 mm, drilled with a drill-bit size of 215.9 mm), high ultrasonic amplitude, and smooth borehole walls, as indicated by the uniform travel time image. UAF1 appears differently when drilled by different drill bits: the amplitude image appears more homogeneous over the intervals drilled with the PDC-type drill bit than with the tricone IADC-type bit, as seen on overlapping sections of logs (see supporting information).
2. UAF2 has low caliper values (220–225 mm) and moderate ultrasonic amplitude; the amplitude image has a texture that appears thinly foliated.
3. UAF3 has higher caliper values (>225 mm) and low ultrasonic amplitude which appears grainy.

## 4. Discussion

### 4.1. Feature Set 1 (FS1): Foliation Planes and Foliation-Parallel Fractures

FS1 features, oriented 60°/145° on average, are interpreted to be foliation planes, deformed foliation-parallel veins, and/or other foliation-parallel fractures. Indeed, FS1 feature orientations are similar to foliation orientations measured on scarce exposures in the Whataroa valley (Figures 1 and 2; Little et al., 2002; Toy et al., 2017), on more extensive outcrops at Tatare Stream (Gillam et al., 2013) and the Amethyst hydroproject (Williams et al., 2018). The progressive deviation of the borehole with depth, to an orientation nearly orthogonal to FS1, is consistent with the effects of drilling through a layered rock mass causing mechanical anisotropy (Misra et al., 2015).

The appearance of the FS1 features, which comprises nearly all of type B and C features, have morphological characteristics consistent with foliation planes. The hangingwall protolith outcropping at Whataroa is strongly foliated (Figures 7a and 7b) with millimeter-to-centimeter-spaced laminae of quartz-feldspar and mica (Little et al., 2002; Toy et al., 2015). The wall rock drill core recovered at 476 m reveals 2–4 mm spaced foliation overprinted by brittle fractures generally at low angle to the foliation; some of these fractures may be drilling-induced (Toy et al., 2017). Type A features that are part of FS1 are interpreted as foliation-parallel,
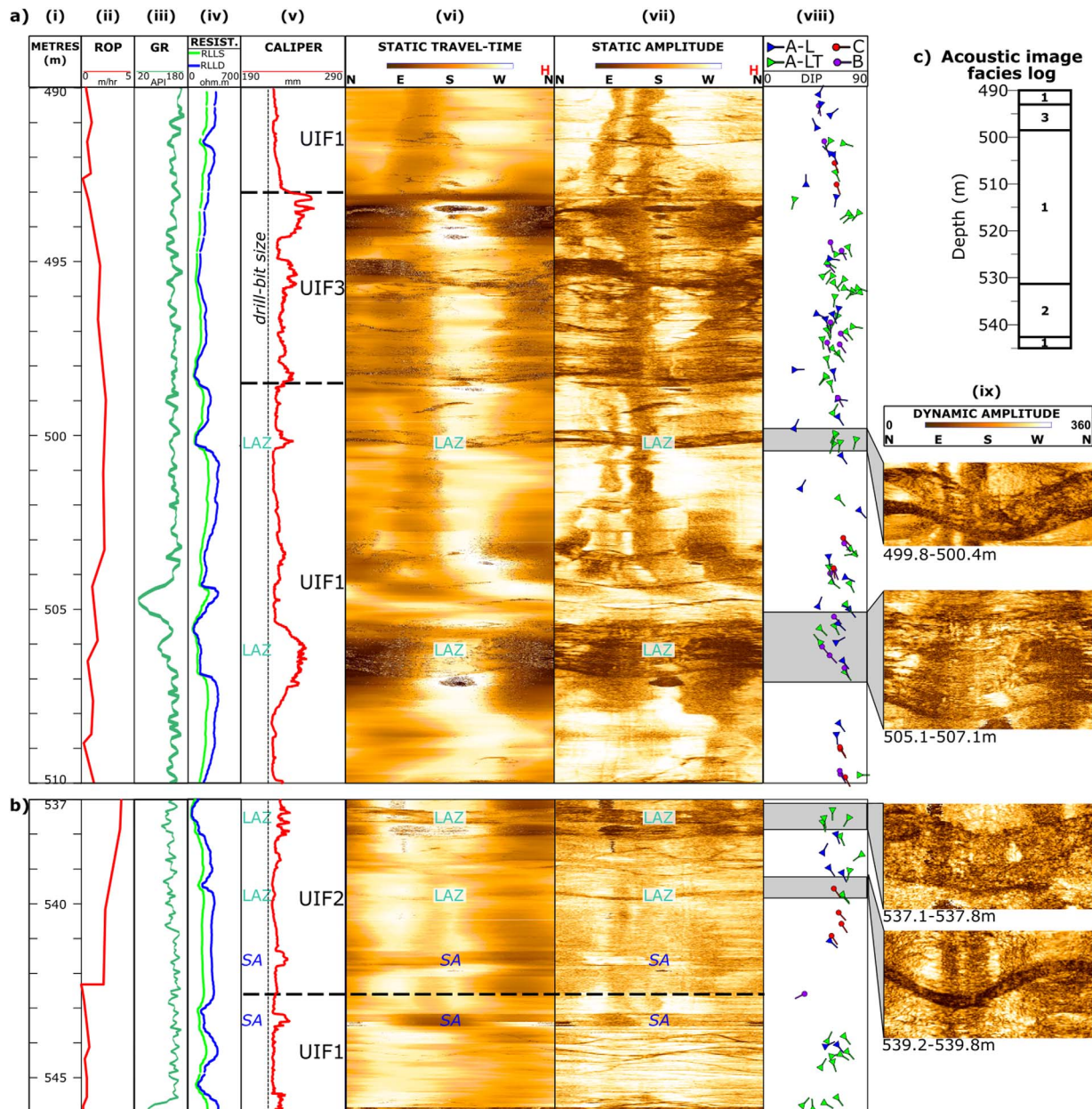
**Figure 6.** Appearance of ultrasonic image facies (UAF) and low-amplitude zones (LAZ). (a) 490–510 m. (b) 537–546 m. (i) depth; (ii) drilling rate of penetration; (iii) natural gamma-ray (GR); (iv) Laterolog (shallow (RLLS) and deep (RLLD) resistivity); (v) caliper calculated from travel time, and drill-bit size; (vi) static travel time BHTV image; (vii) static amplitude BHTV image; (viii) features orientation (tadpole tail indicates the dip direction; see Table 1 for acronyms); (ix) dynamic amplitude BHTV image showing enlargements of LAZ. Note the brecciated texture with angular-shaped centimetric patches of high ultrasonic amplitude in the low-amplitude zones. (c) Summary log of the distribution of the three UAF in the 490–545 m interval. "SA": artifact caused by a drill string stabilizer (supporting information).

centimeter-scale mineral segregations (micaceous or quartz-rich layers), and foliation-parallel veins or fractures. The various degrees of ultrasonic contrast of FS1 features likely relate to changes in mineralogy, or the strength of each layer, which alters the roughness of the borehole wall. The type A-LT features have a high roughness at the borehole wall, and may thus represent slightly excavated mica-rich foliation layers or open fractures. The three type A-H partial features are interpreted to be short quartz veins intercalated with the foliation, as commonly observed in outcrops (Holm et al., 1989; Little et al., 2002) and in the drill core (Toy et al., 2017). Although the transition between protomylonite and mylonite is not clear on the BHTV log, the appearance of the foliation on the BHTV image from the lower interval (>810 m) of DFDP-2B is similar to that in DFDP-1B.
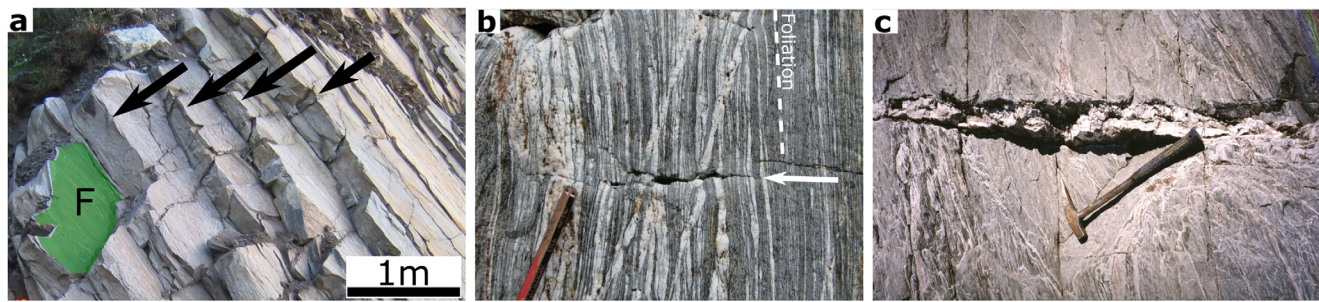
**Figure 7.** Photographs of foliated Alpine Schists, with fractures and veins interpreted to be similar to those in the BHTV log. (a) Foliation planes (green shaded plane "F" and other parallel planes), and steeply dipping foliation-orthogonal joints (arrows) in nonmylonitic Alpine Schist exposed in the Whanganui River quarry, 20 km north of Whataroa. Such exhumation-related brittle structures are common in outcrops of Alpine Fault hangingwall. (b) Open, subhorizontal extension fracture (white arrow) cutting steeply dipping garnet zone schists at Franz Josef Glacier. (c) Gently dipping gash vein from the upper Franz Josef Glacier Valley in biotite zone Alpine schists. This open-cavity vein is infilled by quartz + calcite + chlorite + adularia.

### 4.2. Foliation Orientation: Implications for the Alpine Fault Geometry

Structural studies on outcrops reveal that the active Alpine Fault plane bounds a very high-strain mylonite zone characterized by finite simple shear strains exceeding 120 across most of its <300 m width (Norris & Cooper, 2003; Toy et al., 2013). At such high finite strains, the mylonitic foliation is expected to become essentially parallel to the shear zone boundary (Toy et al., 2013). Previous outcrop studies in the central Southern Alps (including in and near the Whataroa Valley) indicate that the mean attitude of mylonitic foliation within ∼1 km of the Alpine Fault plane is essentially parallel to the Alpine Fault, although in detail such parallelism does not exist everywhere at shorter spatial scales, for example, adjacent to zones of duplexing in the mylonitic zone (Norris & Cooper, 1997). Along-strike of the fault, the mean dip angle of the foliation varies between ∼30 and 60° within a few kilometers (Little et al., 2016). These changes seem to correlate with along-strike changes in the near-surface segmentation of the fault, which is characterized by shallower oblique-thrust segments; and steeper, linking strike-slip segments, which are inferred to merge at depth into a master fault zone (Barth et al., 2012; Norris & Cooper, 1995, 1997). At the (outcrop) scale of observation, the local orientation of the mylonitic foliation is more variable as there it is commonly complicated by late-stage kinking, thrust duplexing, further brittle deformation, which locally steepens the dip; and gravitational collapse of the scarp, which decreases the dip (e.g., Norris & Cooper, 1997). A typical example of this 1–10 m outcrop-scale variability and near-surface segmentation is at Gaunt Creek, where in outcrop the Alpine Fault plane is 43°/105° and the first 100 m structural thickness of the hangingwall contains a wide variety of foliation attitudes/orientations within packages bounded by late listric faults (Cooper & Norris, 1994). There, the local dip of the fault plane is also the dominant feature orientation in DFDP-1B BHTV (Townend et al., 2013; Figure 5d). This supports the argument that except for the local and outcrop-scale discordances, the mylonitic foliation and Alpine Fault plane are approximately parallel to one another. Thus, the 20° lower dip magnitude and 35° dip direction difference between the dominant feature orientations in borehole DFDP-2B (i.e., FS1) versus in DFDP-1B (Figure 5) are not unexpected.

In the DFDP-2B borehole, we have documented a constant foliation orientation with an average dip of 60° toward the SE (dip direction 145°) throughout the protomylonitic to mylonitic hangingwall of the Alpine Fault. This result is significant. About 30 km SW of the DFDP-2B site, in Tatare Stream, a similarly uniform foliation attitude of ∼60° was observed in protomylonitic to mylonitic outcrops (Gillam et al., 2013). Both Tatare Stream and the DFDP-2B borehole in Whataroa Valley encompass large structural data sets, sample the hangingwall's mylonite zone, and both are located near the SW end of an oblique-thrust segment of the Alpine Fault, just east of where the fault transitions westwardly into a strike-slip segment. In the fault segmentation model of Norris and Cooper (1997), and confirmed by recent 3-D mechanical modeling (Upton et al., 2018), such a position is predicted to (uniquely) expose a part of the Alpine Fault that is coplanar with the fault plane at depth that lies below the near-surface zone of segmentation. In Tatare Stream, Gillam et al. (2013) interpreted the uniformity of foliation dip as indicating that the mean SE dip of the Alpine Fault at depth in the central Southern Alps (also its ductile shear zone) was ∼60° (see also Little et al., 2005). Based on the assumption that the mean foliation is parallel to the fault plane, a similar

interpretation is made here for the DFDP-2B site in the Whataroa Valley on the basis of the BHTV data (Figure 2), though the confirmation of this configuration awaits further drilling.

### 4.3. FS2 and FS3: Joints Formed During Exhumation, and Inherited Hydrofractures

The different morphologies of features of FS1 and FS2/FS3 orientations observed in the BHTV log support the interpretation that the latter structures are joints, i.e., structures propagating in opening-mode I in a direction orthogonal to $\sigma_3$, susceptible to having terminations on hard, compliant foliation layers. Most truncated features have FS2/FS3 orientations and are truncated by features of FS1 orientation, while the opposite (features of FS1 orientation stopping either on FS2's or FS3's) is rarely observed (Table 3). Situations in which features of the same set terminate on each other also occur, albeit not commonly. While it is possible that the truncated features were formed by separation and slip on the truncating feature (thus indicating a fault), it would have required a large offset ($>$0.1 m) to not be detected, which is unlikely for all 67 truncated features. Poor image quality hinders the identification of partial features (true or truncated) in the lower part of the logged interval where FS3 is more common, so the intersection configurations of FS3 cannot be described in as much detail as for FS2.

Based on outcrop observation of joints of similar orientation, FS2 features (subvertical and striking NW-SE) are interpreted as joints, probably Neogene, and formed during exhumation. Extension fractures striking NW-SE were documented by Norris and Cooper (1986) in glaciated scoured surfaces in the nearby Franz Josef and Fox valleys, where they were interpreted to have slipped as confining pressure was relieved during glacial unloading in the 1900s. Their kinematic analysis yielded shortening directions consistent with geodetic and micro-earthquake studies, hence representative of tectonic stresses rather than locally induced stresses. NW-SE subvertical extension features were also documented by Hanson et al. (1990). They often form at 90° to the foliation and terminate against foliation planes, which is observed in the BHTV log with FS2 features truncated on foliation planes and foliation-parallel fractures, and FS2 oriented 90° from FS1 (Figures 5 and 7a). In outcrop, such exhumation-related joints are very straight, generally not mineralized, and have lengths of up to tens of meters, which may be the case for FS2 joints, although it is not possible to confirm it solely from borehole data.

FS3 features (gently dipping) are interpreted as inherited hydrofractures or veins. Such gently dipping structures are observed in outcrop in the central Southern Alps (Figures 7b and 7c). Wightman and Little (2007) documented a similar attitude for variably infilled, opening-mode veins in the upper Franz Josef Glacier Valley. These are variably infilled by hydrothermal quartz + calcite + chlorite ± adularia (see also Craw, 1988 and Craw, 1997).

The change in the proportions of FS2 and FS3 joints that takes place at 480–540 m (Figure 3), with FS2 (subvertical) joints more common above this interval and FS3 (gently dipping) inherited hydrofractures more common below, is unlikely to be an artifact. Indeed, the orientation of FS1 features is constant throughout the logged interval, ruling out a significant error of the caliper log (and hence in the calculation of feature orientations); both FS2 and FS3 are present throughout the logged interval; and the change of proportion of FS2 and FS3 occurs within a zone of moderate to good image quality. The top of this transition zone at 470–480 m is also conspicuous in other wireline logs (Sutherland et al., 2015; Townend et al., 2017). Resistivity values are lower, the full-waveform sonic log shows a lower amplitude, the gamma-ray values are lower in the 330–475 m interval than in the 475–888 m interval (Figure 3), and there is a large temperature anomaly at 478 m (Janku-Capova et al., 2018). These log variations reflect lithological or in situ fluid property changes (Li et al., 2014; Rider, 1996). The cause for the change of proportion between FS2 and FS3 at ~500 m is not clear. Joints of FS2 orientation may have a higher ultrasonic impedance contrast with the background formation in the shallow parts of the borehole, thus favoring their identification, while the converse may happen to FS3. However, if this were the case, a more gradual change of proportion would be expected, and would not occur at the same depth as the other wireline log changes. Alternatively, local changes of in situ stresses or pore pressure at deeper depth than the DFDP-2B may have favored the formation of gently dipping hydrofractures in certain zones subsequently exhumed. The preferential near-surface location of subvertical extension fractures may also be related to the remnant effects of deglaciation and rebound which favors NW-SE-striking extension near surface as described by Norris and Cooper (1986), in a stress regime where $\sigma_2 \approx \sigma_3$. Future research dedicated to the examination of the relationships between exhumation-related joints and inherited hydrofractures in outcrops may help to explain these observations.

BHTV log interpretation in DFDP-1B borehole reveals the presence of a secondary feature set dipping moderately north, subperpendicular to the dominant orientation that we suggest represents the foliation (Figure 5d; Townend et al., 2013). This configuration is similar to the FS2 joints striking subperpendicular to FS1 (foliation) observed in the DFDP-2B borehole. A comparison of BHTV logs and cores in a future borehole drilled at a similar distance to the Alpine Fault would provide further information regarding the nature (mineralization, opening, generation) of FS2 and FS3 features in DFDP-2B.

### 4.4. Subsidiary Fault Zones in the Alpine Fault Hangingwall

We interpret the low-amplitude zones with brecciated structures described in section 3.5 to be damage zones associated with subsidiary faults of the Alpine Fault. Similar patterns have been observed on BHTV logs in DFDP-1B, and are correlated to cataclasite zones in cores (Williams, 2017; Williams et al., 2018). Cataclastic shears and gouge-filled zones occur throughout the 1 km-wide fault zone (Norris & Cooper, 2007). Daniel et al. (2004) reported analogous bed-contained brecciated layers inferred from resistivity and BHTV image logs, and correlated to cores in the AIG10 borehole, Gulf of Corinth. In DFDP-2B, clay minerals formed during pervasive alteration from hydrothermal fluids circulating along those type A fractures which, in these zones, would be permeable, may cause the diffuse low ultrasonic amplitudes, as observed in the Amethyst Hydroproject tunnel (Cox & Sutherland, 2007; Figure 1) and at the Soultz geothermal field (France; Genter & Traineau, 1996).

Pelitic-rich or mica-rich zones could also appear as diffuse low ultrasonic amplitudes, but the presence of type A features, the limited depth interval within which they occur, and the brecciated appearance, favors the interpretation of these zones as brecciated fault zones. The low ultrasonic amplitude zones contained between FS1 features may represent foliation-parallel cataclasite zones along which fluid circulation is contained between two specific fracture planes, while those not contained between specific features may result from the percolation of fluids from one or several fractures. The inference that subsidiary faults occur in the hangingwall is consistent with the observation of subsidiary faults in outcrops to the south-east of the main Alpine Fault plane (Hanson et al., 1990; Cox & Sutherland, 2007; Norris & Cooper, 2007; Williams, 2017; Williams et al., 2018). If slip occurs on these structures, they may also generate small earthquakes (Boese et al., 2012; Bourguignon et al., 2015; Chamberlain et al., 2017; Toy et al., 2011).

No significant feature could be identified on the BHTV log at 730 m, where a sharp decrease of static temperature gradient suggests a change of hydrological regime, associated with drilling mud losses while drilling (Figure 8; Sutherland et al., 2015, 2017). Measurements made following drilling of the DFDP-1A and DFDP-1B boreholes demonstrated that a few centimeters of clay gouge is sufficient to create an impermeable barrier to flow, with a difference of three orders of magnitude in permeability measured either side of the principal slip zone of the Alpine Fault (Sutherland et al., 2012). Similar observations have been made at other fault drilling projects (e.g., Li et al., 2013). It is possible that a centimeter-thick, clay gouge layer occurs at ~730 m in DFDP-2B but is not resolved on the BHTV logs. Zones of poor BHTV log quality at 728 and 732 m may represent the damage zone of a low-permeability fault responsible for this major temperature gradient change (Figure 8). Similarly, the lack of low ultrasonic amplitude zones below 558 m is likely caused by the overall poorer BHTV log quality rather than their absence in the rock.

### 4.5. Lithological Variability Within the Hangingwall of the Alpine Fault

Hard formations, and some minerals including quartz or calcite, tend to have lower caliper values and higher ultrasonic amplitude than softer formations or clay and micas minerals, due to their higher ultrasonic impedance and lower roughness at the borehole wall (Massiot et al., 2015; Zemanek et al., 1970). We interpret the nature of the three ultrasonic image facies delineated in the 490–545 m interval (section 3.5) based on these relationships.

The ultrasonic image facies UAF1 and UAF2 are inferred to be hard, quartz-rich formations as indicated by their high ultrasonic amplitude and low caliper, with UAF2 appearing more thinly foliated or grainy than UAF1. This inference is also supported by the presence of hard layers which wore out the drill bits and slowed down the drilling progress in the 519–524 m interval and at 546.8 m, both within UAF1. The rate of penetration of the drill bit is high between 527 and 543 m, similar to the interval where UAF2 occurs, suggesting that there are fewer hard quartz veins (Figure 6). Thus, the lithology corresponding to UAF1 may be harder and contain more, thicker, or more continuous quartz veins than UAF2. The gamma-ray log does not
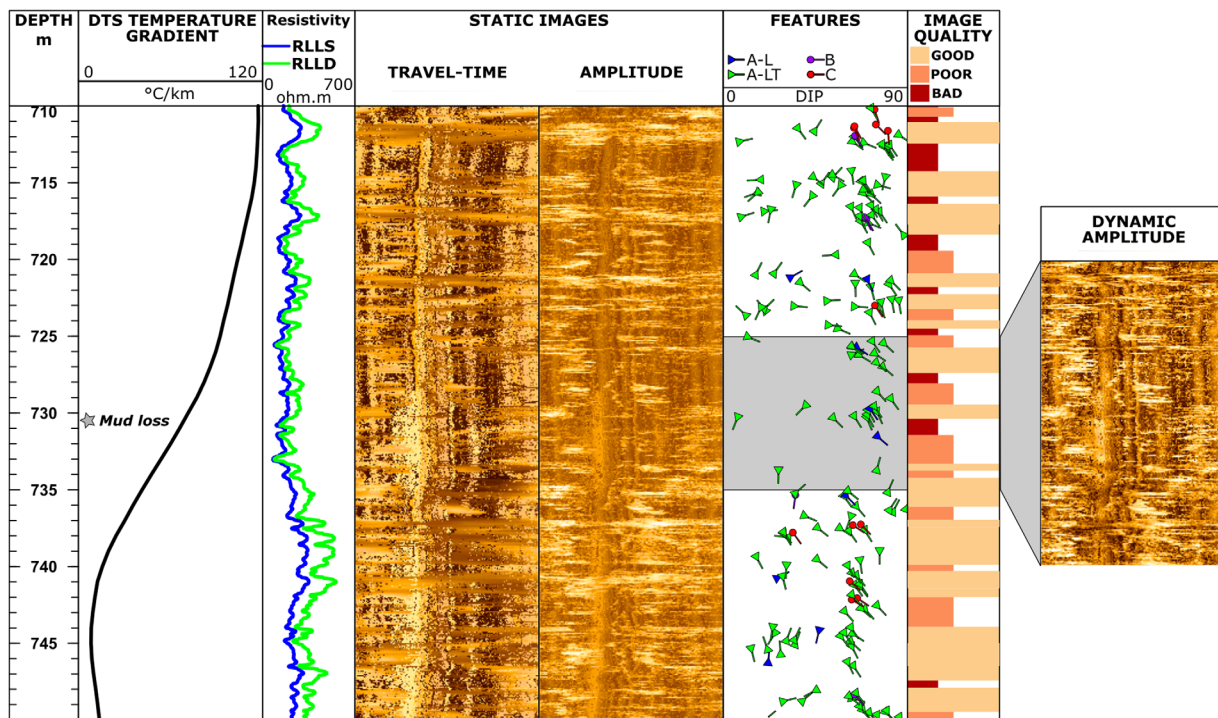
**Figure 8.** BHTV log of the 710–750 m interval surrounding a major static temperature gradient change and mud loss while drilling, showing numerous thin intervals of bad and poor image quality within intervals of good image quality which may indicate intensely fractured zones. From left to right: depth, static temperature gradient from distributed temperature sensing (DTS) cable, resistivity, static travel time image, static amplitude image, tadpoles of interpreted features, BHTV log quality, dynamic amplitude image enlargement of the 725–735 m interval surrounding the sharp decrease in temperature gradient and mud loss zone.

provide meaningful information at this depth. A very low gamma-ray and high deep resistivity anomaly is observed on multiple logging runs at 504–505.5 m, which could indicate a low-mica or low-clay zone, and conversely a high-quartz zone. This interval has a high ultrasonic amplitude and low caliper, similar to the characteristic of UAF1.

UAF3 (493–498.5 m) is a softer formation with higher borehole wall roughness than UAF1/UAF2, and may contain more mica and/or clay minerals as indicated by the lower ultrasonic amplitude. The UAF3 interval is associated with a low resistivity which may be caused by a clay-rich or mica-rich formation, and/or by a higher fluid content. The latter is consistent with the high density of type A features observed in UAF3 which may be permeable fractures.

While we were able to describe ultrasonic image facies in detail only on a 55 m long interval of the logged interval, image log facies highlight local variations in quartz:mica content or in alteration which cannot be identified from cuttings alone, sampled only every 2 m and subject to mixing within the borehole. The possible variations of mineralogy, rock hardness or layering style that we have interpreted here may cause 1–10 m scale variations in formation strength and anisotropy along the borehole. These variations likely occur in other locations in the hangingwall of the Alpine Fault and may also locally impact the fracture distribution, as observed in outcrops (Williams et al., 2018).

### 4.6. Potential for Fracture Slip in the Hangingwall of the Alpine Fault

The occurrence of joints of both FS2 and FS3 orientations is consistent with a stress regime at the time of crack formation during exhumation in which the intermediate and minimum compressive stresses ($\sigma_2$ and $\sigma_3$, respectively) were of similar magnitudes. This would facilitate a switch from subvertical $\sigma_2$ (a strike-slip regime, as determined from focal mechanism inversions; Boese et al., 2012) to subvertical $\sigma_3$ and NE-SW-trending $\sigma_2$ (a reverse faulting regime), locally and/or transiently. Geological observations along the central Alpine Fault suggest such a stress configuration prevails near the brittle-ductile transition (Little et al., 2016); at ~3 km depth (Holm et al., 1989); and near the surface due to late-stage exhumation and deglaciation (Hanson et al., 1990; Norris & Copper, 1986).

Switching between $\sigma_2$ and $\sigma_3$ has previously been interpreted to be possibly related to a postseismic transient stress rotations, or stress perturbations close to active faults (Little et al., 2016). In addition, recent numerical stress modeling of topographic and tectonic stresses shows that $\sigma_2$ is currently rotated by topographic relief from near-vertical under the ridges to near-horizontal beneath valleys crossing the Alpine fault (such as the Whataroa Valley), resulting in a thrust stress regime rather than oblique strike-slip (Figure 9; Upton et al., 2018). In the models, tectonic stresses in the hanging wall combined with slope-generated stresses have formed a reverse fault extending ca. 10 km along the western Whataroa valley, near the location of DFDP-2B.

To examine the present-day proximity to shear failure of fractures observed in DFDP-2B, we have estimated stress magnitudes assuming both strike-slip and reverse stress regimes at frictional-failure equilibrium (Zoback & Townend, 2001). We adopt a low stress ratio of $\varphi = (\sigma_2 - \sigma_3)/(\sigma_1 - \sigma_3) = 0.15$ and a horizontal orientation with a trend of 115° for the $\sigma_1$ axis. The frictional-failure criterion can be written as

$$\frac{S_1 - Pp}{S_3 - Pp} = \frac{\sigma_1}{\sigma_3} = \left(\sqrt{\mu^2 + 1} + \mu\right)^2 \tag{1}$$

where

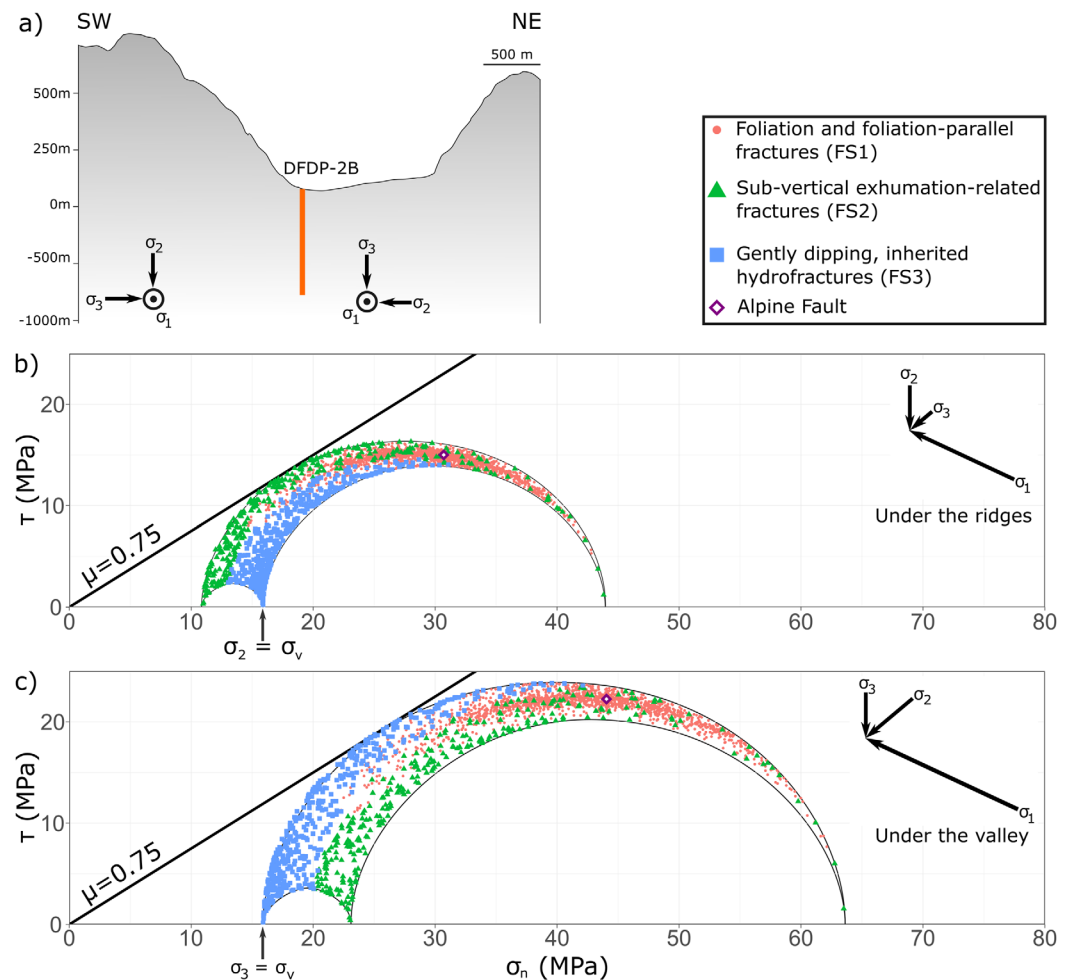$$P_p = \lambda S_v = \lambda \rho g z \tag{2}$$



**Figure 9.** Mohr circles of all features identified in DFDP-2B and the Alpine Fault assuming a critically stressed regime with $\Phi = 0.15$, and principal stress directions compatible with those obtained in Upton et al. (2018). Stresses estimated at 1 km depth with $\sigma_1$ horizontal and oriented 115°. (a) Elevation profile across the Whataroa Valley with diagrams of the two simplified numerically modeled stress regimes. (b) Strike-slip regime, under the ridges. (c) Reverse regime, under the valleys. DFDP-2B is located on the side a the Whataroa Valley near a steep ridge.

Here $\mu$ is the coefficient of friction, $P_p$ the pore fluid pressure, $\lambda$ the pore fluid factor, $S_v$ the vertical stress, $g$ the gravitational acceleration, $\rho$ the mean rock density, and $z$ the depth. The Mohr circles are presented after solving for the three principal stresses using $\mu = 0.75$, $\lambda = 0.4$, $\rho = 2,700$ kg/m$^3$, and $z = 1$ km (Figure 9). The resulting stress magnitudes are consistent with those estimated by Upton et al. (2018). While the $\sigma_1$ orientation adopted in this simple model is that computed for seismogenic depths (Boese et al., 2012), numerical models reveal a similar orientation of $\sigma_1$ in the Whataroa valley (Upton et al., 2018). The precise determination of the stress tensor in DFDP-2B awaits further high-resolution modeling.

In each of the two stress configurations considered, the foliation and foliation-parallel FS1 features, including the Alpine Fault plane, are not well-oriented for shear failure. On the other hand, subvertical joints (FS2) are close to failure in the strike-slip regime, and gently dipping (FS3) in the reverse regime. In addition, principal stress directions are not purely vertical and horizontal (Boese et al., 2012; Little et al., 2016; Upton et al., 2018), so the spread around the mean of fracture orientations will cause different fractures to be close to failure depending on the stress tensor at the precise fracture location. In other words, the subsidiary FS2 and FS3 fracture orientations observed in the DFDP-2B borehole combined with low ambient stress ratios thus provide pervasive fractures subject to frictional failure under the combined local effects of topographic and tectonic loading. High relief locally enhances the potential for switching between $\sigma_2$ and $\sigma_3$ (Upton et al., 2018).

### 4.7. Implications for Fracture Permeability Adjacent to a Plate Boundary Fault With High Topography

An exhaustive analysis of the relationship between fracture orientation and permeability is beyond the scope of this study, but inferences can be made on potential fluid flow directions in the hangingwall of the Alpine Fault. Regrettably, it was not possible to carry out hydraulic packer testing to estimate formation permeability (Sutherland et al., 2015).

Among the various features, type A-LT features are the most likely to be permeable as they locally increase roughness at the borehole wall, though it is not known how far these fractures propagate into the formation. The zones of low ultrasonic amplitude interpreted to be subsidiary faults with damage zones, some of them confined within foliation planes and hence subparallel to the Alpine Fault (section 4.4), are good candidates for contributing to permeability in the hangingwall, although they may be partially clogged with clays. A similar interpretation was made from field and DFDP-1B core sample XRD analyses (Williams et al., 2017). The meter-scale zones of poor BHTV log quality between 545 and 888 m may represent densely fractured zones composed from structures of all feature sets (FS1–3) and induce spalling from the borehole wall, and thus may also be permeable.

The pervasive occurrence of FS1 fractures along the borehole, and the change in relative abundance of FS2 and FS3 at 480–550 m, define the fracture system geometry through which fluids circulate in the hangingwall of the Alpine Fault in the Whataroa Valley. At least some of the foliation-parallel fractures (FS1), exhumation-related joints (FS2), and inherited hydrofractures (FS3), are not fully sealed and likely permeable, as seen by temperature gradient and resistivity changes (Figure 10). Foliation-parallel fractures alone would not constitute a well-connected fracture system, but their intersection with fractures of FS2 and FS3 orientations, at high angles to the foliation, would provide the necessary connectivity. The truncation of fractures of FS2 and FS3 orientations on foliation planes are an example of such connections and in places are associated with temperature anomalies (Figure 10).

We infer that flow dominantly occurs within the foliation plane orientation (FS1) based on the dominant orientation of the subsidiary faults observed on the BHTV log, so the direction of minimum permeability is normal to this plane. At the DFDP-2B site, FS2 fractures which predominate above 500 m may connect basement foliation planes vertically with the Quaternary sediments. FS3 fractures, which predominate below 500 m, favor lateral (subhorizontal) connectivity. The intersections of fracture set orientations, potentially forming pipe-like conduits, provides an estimate of the direction of maximum permeability (trend/plunge 135°/60° for FS1/FS2; 063°/13° for FS1/FS3; and to a limited extent 317°/03° for FS2/FS3). The direction of intermediate permeability is normal to the plane defined by maximum and minimum directions. It is, therefore, possible to estimate the three principal directions of the anisotropic permeability tensor.

Large-scale permeability anisotropy caused by the fracture system geometry in the foliated rock mass has also been observed at core scale in the DFDP-1 borehole (Allen et al., 2017), where anisotropy increases
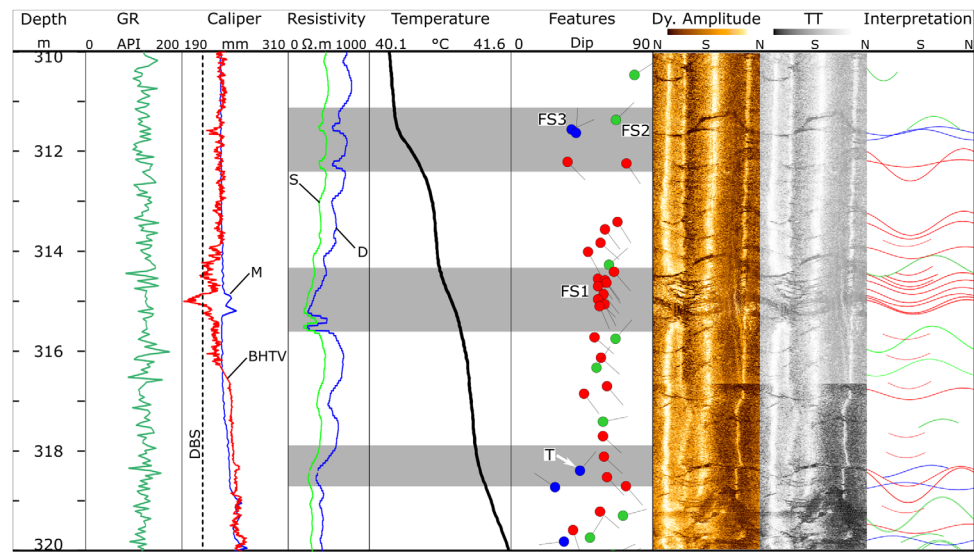
**Figure 10.** Examples of permeable fractures of each orientation set, and at the intersection between a truncated (*T*) FS3 and a continuous FS1 fracture, identified by temperature changes (shaded areas) and consistent with resistivity and in cases caliper log variations. FS1, FS2, and FS3 features are represented as red, green and blue tadpoles, respectively. *From left to right: natural gamma-ray, caliper (DBS: drill-bit size; M: 1-arm caliper; BHTV: calculated from BHTV log), resistivity (S: shallow; D: deep) temperature run 7 h after end of mud circulation (R04_P1; Sutherland et al., 2015), tadpoles of features colored by their orientation, dynamic amplitude, travel time, interpreted sinusoids.*

away from the principal slip zones. Future work will address which of the >2,200 features interpreted from DFDP-2B BHTV logs are permeable, based on analysis of independent data (resistivity, temperature and sonic logs; Janku-Capova et al., 2018). This may further constrain the fracture permeability tensor, but hydraulic tests are required to determine absolute values of permeability.

In addition, reactivation of fractures of FS2 and FS3 orientations, under a strike-slip or reverse faulting regime, respectively, would likely increase their hydraulic conductivity (Barton et al., 1995; Townend & Zoback, 2000). Combined with the connection with foliation-parallel fractures, the fracture architecture observed in borehole DFDP-2B supports the concept of an outer damage zone proposed by Townend et al. (2017) of enhanced fracture-controlled permeability ($10^{-16}$ to $10^{-13}$ m$^2$) into the Alpine Fault's hangingwall (Cox et al., 2015; Sutherland et al., 2017; Townend et al., 2017). Stress effects may enhance vertical permeability below the ridges, and lateral permeability below the valleys, near the Alpine Fault and other active faults of high topographic relief, though this hypothesis awaits confirmation from further high-resolution stress and fluid flow models.

## 5. Conclusion

The interpretation of BHTV logs acquired in the DFDP-2B borehole yields a detailed and continuous record of foliation and fractures in the hangingwall of the central Alpine Fault. The constant foliation dip of 60° towards 145° observed in the borehole is similar to that observed in outcrop in the nearby Tatare Valley, and suggests that the dextral-reverse Alpine Fault plane here dips ~60° SE. Outcrop observations support the interpretation that auxiliary FS2 (subvertical striking NW-SE, and mainly above ~500 m) and FS3 (gently dipping, and mainly below ~500 m) fracture sets represent exhumation joints and inherited hydrofractures, respectively. The orientation of these joints is consistent with inferred paleostress orientations, and magnitudes $\sigma_2 \approx \sigma_3$. The presence of three ultrasonic image facies over a 50 m long interval highlights local variability in lithology and/or alteration, which is also consistent with nearby outcrop observations and likely affect mechanical rock properties and the fracture system architecture. Together with a series of brecciated altered subsidiary faults, we suggest that foliation-parallel fractures (especially those features visible on the travel time image) and the two auxiliary fracture sets define the fracture network controlling fluid flow within the Alpine Fault's hangingwall in the Whataroa Valley. The resulting permeability tensor near the DFDP-2B borehole is thus likely anisotropic with fluid flow dominantly occurring along abundant foliation-

**Table A1**

*List of BHTV Logs Used in This Study With Related Depth Shift During Depth Matching (Positive Values Indicate a Downward Depth Shift), Depth Intervals After Depth Matching, Mean Borehole Azimuth and Deviation, and Overall BHTV Log Quality*

| Tool | Log | Shift (m) | Top depth (m) | Bottom depth (m) | Hole azimuth (°) | Hole deviation (°) | BHTV quality |
|------|-----|-----------|---------------|------------------|------------------|--------------------|--------------|
| ABI40 | R02P4 | 0.3953 | 260 | 275.15 | 217.06 | 2.8 | Good |
| | R11P3 | 0.2503 | 275.15 | 316.33 | 300.29 | 2.2 | Good |
| | R26P6 | −0.1547 | 316.33 | 341.35 | 334.76 | 3.9 | Poor-good |
| | R26P7 | −0.1547 | 341.35 | 383.73 | 343.37 | 7.7 | Poor-good |
| | R28P6 | 0.0953 | 383.73 | 457.3 | 345.25 | 13.5 | Poor-good |
| | R28P5 | 0.0953 | 457.3 | 465.6 | 345.17 | 16.1 | Good |
| | R28P4 | 0.0953 | 465.6 | 476.6 | 345.85 | 16.4 | Good |
| | R37P2 | −0.0047 | 476.6 | 523.7 | 347.42 | 18.7 | Good (locally bad) |
| | R39P1 | −0.0453 | 523.7 | 545.86 | 344.52 | 22.3 | Good |
| ABI43 | R47P9 | 0.3953 | 545.86 | 797.85 | 343.18 | 34.8 | Bad-good |
| | R51P13 | 1.0453 | 797.85 | 818.15 | 340.08 | 42.3 | Bad-good |
| | R51P11 | 1.0453 | 818.15 | 884.75 | 340.67 | 43.5 | Bad-good |
| | R51P09 | 1.0453 | 884.75 | 888 | 340.61 | 44.9 | Bad-good |

*Note.* The log names refer to Sutherland et al. (2015), depth intervals are measured along the borehole after depth matching, azimuth is relative to geographic north and deviation to vertical.

parallel fractures, complemented by additional pathways that are subvertical above 500 m and gently dipping below. The two auxiliary fracture sets are well-oriented for reactivation under strike-slip and reverse faulting regimes, caused by the combination of tectonic, topographic and late-exhumation-related stresses. The strong variations of relief along-strike of the Alpine Fault enhances vertical flow under the ridges, and lateral flow under the valleys. Thus, the high fracture density, variable fracture orientations observed in the BHTV logs, together with a stress tensor perturbed by topographic relief, support a model of an outer damage zone of enhanced permeability along critically stressed fractures.



**Figure A1.** Example of caliper calculation from BHTV log, with the fitted circle, travel time measurements around the borehole, and upper and lower bounds of the window time (136 and 157 $\mu$s in this case). Points within the inner green circle or outside the outer green circle were arbitrarily assigned to the window time bounds during logging and not used for fitting the circle. Circle fitting is made on the raw measurement in microseconds (radial coordinates), the circular orientation reference is arbitrary. The fitted circle center (red cross) indicates here a slight decentralization.

## Appendix A: BHTV Log Acquisition and Processing

Two ultrasonic imaging (BHTV) tools developed by Advanced Logic Technology were used to accommodate the high temperatures encountered in DFDP-2B (Sutherland et al., 2015): the ABI40® in the 260–545.86 m interval and the ABI43® in the 545.86–888 m interval, able to operate at a temperature up to 70°C and 125°C, respectively (Table A1). Both tools emit pulses with a 1.2 MHz frequency. Logs recorded 288 data points per revolution with 2 mm depth increments, at logging speeds of 0.5–1.2 m/min. The resulting image pixel size is ∼4 × 2 mm in the sections drilled with a 241.3 mm (9.5 in) and 215.9 mm (8.5 in) diameter drill bits (264–274.9 and 274.9–893 m intervals, respectively). The ultrasonic wave travel time and amplitude are converted into images oriented with respect to magnetic north and vertical using an in-built three-components accelerometer and magnetometer. These sensors also allow to monitor borehole deviation and azimuth. The data set is corrected for both the 23.15°E magnetic declination and the borehole deviation.

BHTV logs acquired with the ABI40 tool were depth-matched with other wireline logs using the gamma-ray sensors included as part of each logging tool suites (Sutherland et al., 2015). The ABI43 tool was not stackable with the available gamma-ray tool, and hence the deepest logs acquired with this tool were adjusted by matching successive overlapping sections.
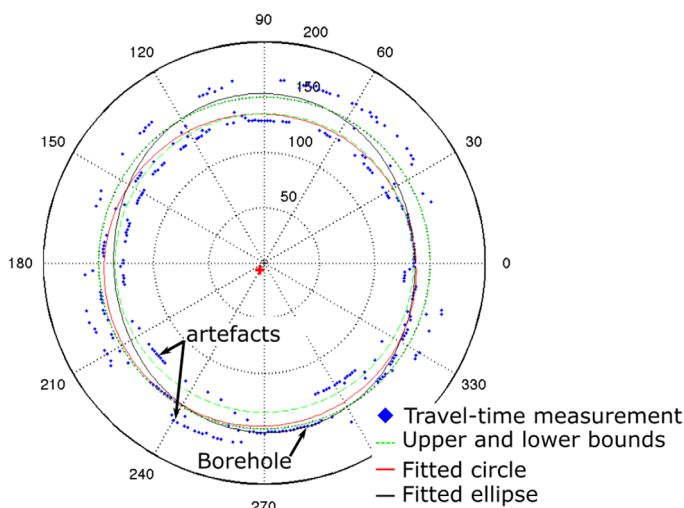
The raw BHTV logs and associated acquisition curves were exported from WellCAD™ and processed in Recall™ 5.4. Two classic types of image normalizations were used to enhance the image (Rider, 1996): (1) static, which normalizes travel time and amplitude values over the entire log and highlights large-scale variations (>1 m), and (2) dynamic, which normalizes the images over a moving window of given width (0.5 m depth in our case) and highlights local variations.

### Appendix B: Calculations of Borehole Diameter (Caliper)

The first step of the caliper calculation from the BHTV travel time consists of evaluating the borehole's diameter in the time domain for each depth increment. For each depth increment, a circle was fitted to BHTV travel time logs acquired with the ABI40 tool. Logs acquired with the ABI43 (546–888 m) had less signal returned, so the circle was fitted on travel time data set of five successive scans (i.e., every centimeter) to increase signal:noise ratio, based on the assumption that the caliper is unlikely to vary significantly over 1 cm (Figure A1). To ensure the circle fitted the formation signal and not the internal tool reflections, we imposed minimum and maximum diameters corresponding to the limits of the window time. A fit was deemed good when at least 75% of the points satisfied this limit. This method limits false detection of tool noise rather than echoes back from the borehole wall. The main limitation of this procedure, however, is its inability to capture diameters larger or smaller than the window time.

The second step of the caliper calculation consists of converting the diameter from time into distance. The speed of sound in the mud was evaluated using thermodynamic equations (Wagner & Kretzschmar, 2007) taking into account temperatures and pressures recorded at each logging depth, and time spent within the tool itself. As there were no temperature sensors on the ABI tools, temperature logs acquired just prior to each BHTV logging run were used as proxies. Additionally, a coefficient related to the mud density measured at the outflow from the borehole was made to take into account changes in mud properties. The resulting caliper measurements were validated in the steel casing of known diameter, in sections of the borehole with high signal to noise return, and with a three-arm mechanical caliper log acquired in the upper part of the hole (264–395 m; Figure 3). Unfortunately, the mechanical caliper tool was not reliable in deeper sections of the borehole (Sutherland et al., 2015).

The quality of the caliper log calculated from the BHTV travel time relates directly to the BHTV quality: moderate between 260 and 476 m, very good between 476 and 545.86 m, variable between 545.86 and 558 m, bad between 558 and 598 m and variable between 598 and 888 m. A bad caliper quality indicates that the caliper may not represent the actual borehole shape. In intervals of bad caliper quality, the caliper log is ~10 mm bigger than the drill-bit size due to the upper limit allowed on the borehole diameter. While this estimation likely underestimates borehole enlargements where return signal is poor, it remains a better proxy for borehole diameter than a constant bit size that would lead to an overestimation of structural dips in enlarged intervals.

### References

Allen, M. J., Tatham, D., Faulkner, D. R., Mariani, E., & Boulton, C. (2017). Permeability and seismic velocity and their anisotropy across the Alpine Fault, New Zealand: An insight from laboratory measurements on core from the Deep Fault Drilling Project phase 1 (DFDP-1). *Journal of Geophysical Research: Solid Earth*, *122*, 6160–6179. https://doi.org/10.1002/2017JB014355

Barth, N. C., Toy, V. G., Langridge, R. M., & Norris, R. J. (2012). Scale dependence of oblique plate-boundary partitioning: New insights from LiDAR, central Alpine fault, New Zealand. *Lithosphere*, *4*(5), 435–448. https://doi.org/10.1130/L201.1

Barton, C. A., & Zoback, M. D. (1992). Self-similar distribution and properties of macroscopic fractures at depth in crystalline rock in the Cajon Pass Scientic DrillHole. *Journal of Geophysical Research*, *97*(B4), 5181–5200. https://doi.org/10.1029/91jb01674

Barton, C. A., & Zoback, M. D. (2002). Wellbore imaging technologies applied to reservoir geomechanics and environmental engineering. In M. Lovell & N. Parkinson (Eds.), *AAPG methods in exploration: Geological applications of well logs* (Vol. 13, pp. 39–53). Tulsa, OK: The American Association of Petroleum Geologists.

Barton, C. A., Zoback, M. D., & Moos, D. (1995). Fluid flow along potentially active faults in crystalline rock. *Geology*, *23*(8), 683–686. https://doi.org/10.1130/0091-7613(1995)023<0683:FFAPAF>2.3.CO;2

Berryman, K. R., Cochran, U. A., Clark, K. J., Biasi, G. P., Langridge, R. M., & Villamor, P. (2012). Major earthquakes occur regularly on an isolated plate boundary fault. *Science*, *336*(6089), 1690–1694. https://doi.org/10.1126/science.1218959

Blake, K., & Davatzes, N. C. (2012). Borehole image log and statistical analysis of FOH-3D, Fallon Naval Air Station, NV. In *Proceedings of the thirty-seventh workshop on geothermal reservoir engineering*. Stanford, CA: Stanford University.

Boese, C. M., Townend, J., Smith, E., & Stern, T. (2012). Microseismicity and stress in the vicinity of the Alpine Fault, central Southern Alps, New Zealand. *Journal of Geophysical Research*, *117*, B02302. https://doi.org/10.1029/2011JB008460

Boness, N. L., & Zoback, M. D. (2006). A multiscale study of the mechanisms controlling shear velocity anisotropy in the San Andreas Fault Observatory at Depth. *Geophysics*, *71*(5), F131–F146. https://doi.org/10.1190/1.2231107

Boulton, C., Carpenter, B. M., Toy, V., & Marone, C. (2012). Physical properties of surface outcrop cataclastic fault rocks, Alpine Fault, New Zealand. *Geochemistry, Geophysics, Geosystems*, *13*, Q01018. https://doi.org/10.1029/2011GC003872

Bourguignon, S., Bannister, S., Henderson, C. M., Townend, J., & Zhang, H. (2015). Structural heterogeneity of the midcrust adjacent to the central Alpine Fault, New Zealand: Inferences from seismic tomography and seismicity between Harihari and Ross. *Geochemistry, Geophysics, Geosystems*, *16*, 1017–1043. https://doi.org/10.1002/2014GC005702

Brudy, M., & Zoback, M. (1999). Drilling-induced tensile wall-fractures: Implications for determination of in-situ stress orientation and magnitude. *International Journal of Rock Mechanics and Mining Sciences*, *36*(2), 191–215. https://doi.org/10.1016/s0148-9062(98) 00182-x

Burns, K. L. (1987). *Geological structures from Televiewer Logs of GT-2, Fenton Hill, New Mexico* (Tech. Rep. LA-10619-HDR). Los Alamos, NM: Los Alamos National Laboratory.

Caine, J., Evans, J., & Forster, C. (1996). Fault zone architecture and permeability structure. *Geology*, *24*(11), 1025–1028. https://doi.org/10.1130/0091-7613(1996)024<1025:FZAAPS>2.3.CO;2

Carpenter, B., Kitajima, H., Sutherland, R., Townend, J., Toy, V., & Saffer, D. (2014). Hydraulic and acoustic properties of the active Alpine Fault, New Zealand: Laboratory measurements on DFDP-1 drill core. *Earth and Planetary Science Letters*, *390*, 45–51. https://doi.org/10.1016/j.epsl.2013.12.023

Chamberlain, C. J., Boese, C. M., & Townend, J. (2017). Cross-correlation-based detection and characterisation of microseismicity adjacent to the locked, late-interseismic Alpine Fault, South Westland, New Zealand. *Earth and Planetary Science Letters*, *457*, 63–72. https://doi.org/10.1016/j.epsl.2016.09.061

Chester, F. M., Evans, J. P., & Biegel, R. L. (1993). Internal structure and weakening mechanisms of the San Andreas Fault. *Journal of Geophysical Research*, *98*(B1), 771–786. https://doi.org/10.1029/92JB01866

Cochran, U. A., Clark, K. J., Howarth, J. D., Biasi, G. P., Langridge, R. M., Villamor, P., et al. (2017). A plate boundary earthquake record from a wetland adjacent to the Alpine fault in New Zealand refines hazard estimates. *Earth and Planetary Science Letters*, *464*, 175–188. https://doi.org/1016/j.epsl.2017.02.026

Conin, M., Bourlange, S., Henry, P., Boiselet, A., & Gaillot, P. (2014). Distribution of resistive and conductive structures in Nankai accretionary wedge reveals contrasting stress paths. *Tectonophysics*, *611*, 181–191. https://doi.org/10.1016/j.tecto.2013.11.025

Constantinou, A., Schmitt, D. R., Kofman, R., Kellett, R., Eccles, J., Lawton, D., et al. (2016). Comparison of fibre optic sensor and borehole seismometer VSP surveys in a scientific borehole—DFDP-2B, Alpine Fault, New Zealand. In *SEG international exposition and 86th annual meeting* (pp. 5608–5612). Tulsa, US: Society of Exploration Geophysicists. https://doi.org/10.1190/segam2016-13946302.1

Cooper, A. F., & Norris, R. J. (1994). Antatomy, structural evolution, and slip rate of a plate boundary thrust: The Alpine Fault at Gaunt Creek, Westland, New Zealand. *Geological Society of America Bulletin*, *106*(5), 627–633. https://doi.org/10.1130/0016-7606(1994)106<0627:ASEASR>2.3.CO;2

Cox, S. C., Menzies, C. D., Sutherland, R., Denys, P. H., Chamberlain, C., & Teagle, D. A. H. (2015). Changes in hot spring temperature and hydrogeology of the Alpine Fault hanging wall, New Zealand, induced by distal South Island earthquakes. *Geofluids*, *15*(1–2), 216–239. https://doi.org/10.1111/gfl.12093

Cox, S. C., & Sutherland, R. (2007). Regional geological framework of South Island, New Zealand, and its significance for understanding the active plate boundary. In D. Okaya, T. Stern, & F. Davey (Eds.), *A continental plate boundary: Tectonics at South Island, New Zealand* (pp. 19–46). Washington, DC: American Geophysical Union. https://doi.org/10.1029/175GM03

Craw, D. (1988). Shallow-level metamorphic fluids in a high uplift rat metamorphic belt; Alpine Schist, New Zealand. *Journal of Metamorphic Geology*, *6*(1), 1–16. https://doi.org/10.1111/j.1525-1314.1988.tb00405.x

Craw, D. (1997). Fluid inclusion evidence for geothermal structure beneath the Southern Alps, New Zealand. *New Zealand Journal of Geology and Geophysics*, *40*(1), 43–52. https://doi.org/10.1080/00288306.1997.9514739

Daniel, J.-M., Moretti, I., Micarelli, L., Chuyne, S. E., & Piane, C. D. (2004). Macroscopic structural analysis of AG10 well (Gulf of Corinth, Greece). *Comptes Rendus Geoscience*, *336*(4–5), 435–444. https://doi.org/10.1016/j.crte.2004.01.001

Davatzes, N. C., & Hickman, S. H. (2010). Stress, fracture, and fluid-flow analysis using acoustic and electrical image logs in hot fractured granites of the Coso Geothermal Field, California, U.S.A. In M. Poppelreiter, C. Garcia-Carballido, & M. Kraaijveld (Eds.), *Dipmeter and borehole image log technology* (AAPG Memo. 92, pp. 259–293, Special Volumes). Tulsa, OK: American Association of Petroleum Geologists. https://doi.org/10.1306/13181288M923134

Faulkner, D., Jackson, C., Lunn, R., Schlische, R., Shipton, Z., Wibberley, C., et al. (2010). A review of recent developments concerning the structure, mechanics and fluid flow properties of fault zones. *Journal of Structural Geology*, *32*(11), 1557–1575. https://doi.org/10.1016/j.jsg.2010.06.009

Feenstra, J., Thurber, C., Townend, J., Roecker, S., Bannister, S., Boese, C., et al. (2016). Microseismicity and P-wave tomography of the central Alpine Fault, New Zealand. *New Zealand Journal of Geology and Geophysics*, *59*(4), 483–495. https://doi.org/10.1080/00288306.2016.1182561

Genter, A., & Traineau, H. (1996). Analysis of macroscopic fractures in granite in the HDR geothermal well EPS-1, Soultz-sous-Forets, France. *Journal of Volcanology and Geothermal Research*, *72*(1–2), 121–141. https://doi.org/10.1016/0377-0273(95)00070-4

Gillam, B. G., Little, T. A., Smith, E., & Toy, V. G. (2013). Extensional shear band development on the outer margin of the Alpine mylonite zone, Tatare Stream, Southern Alps, New Zealand. *Journal of Structural Geology*, *54*, 1–20. https://doi.org/10.1016/j.jsg.2013.06.010

Hall, K. W., Isaac, H., Bertram, M., Bertram, K., Lawton, D., Constantinou, A., et al. (2017). Always finding faults: New Zealand 2016. In *SEG Annual Meeting*, Houston, 24–29 September. Tulsa, OK: Society of Exploration Geophysicists. https://doi.org/10.1190/segam2017-17664833.1

Hanson, C. R., Norris, R. J., & Cooper, A. F. (1990). Regional fracture patterns east of the Alpine Fault between the Fox and Franz Josef Glaciers, Westland, New Zealand. *New Zealand Journal of Geology and Geophysics*, *33*(4), 617–622. https://doi.org/10.1080/00288306.1990.10421379

Hickman, S., & Zoback, M. (2004). Stress orientations and magnitudes in the SAFOD pilot hole. *Geophysical Research Letters*, *31*, L15S12. https://doi.org/10.1029/2004GL020043

Holm, D., Norris, R., & Craw, D. (1989). Brittle and ductile deformation in a zone of rapid uplift: Central Southern Alps, New Zealand. *Tectonics*, *8*(2), 153–168. https://doi.org/10.1029/TC008i002p00153

Hung, J.-H., Ma, K.-F., Wang, C.-Y., Ito, H., Lin, W., & Yeh, E.-C. (2009). Subsurface structure, physical properties, fault-zone characteristics and stress state in scientific drill holes of Taiwan Chelungpu Fault Drilling Project. *Tectonophysics*, *466*(3–4), 307–321. https://doi.org/10.1016/j.tecto.2007.11.014

Ikari, M. J., Carpenter, B. M., Kopf, A. J., & Marone, C. (2014). Frictional strength, rate-dependence, and healing in DFDP-1 borehole samples from the Alpine Fault, New Zealand. *Tectonophysics*, *630*, 1–8. https://doi.org/10.1016/j.tecto.2014.05.005

Ikari, M. J., Trutner, S., Carpenter, B. M., & Kopf, A. J. (2015). Shear behaviour of DFDP-1 borehole samples from the Alpine Fault, New Zealand, under a wide range of experimental conditions. *International Journal of Earth Sciences*, *104*(6), 1523–1535. https://doi.org/10.1007/s00531-014-1115-5

Ito, H., & Kiguchi, T. (2005). Distribution and properties of fractures in and around the Nojima Fault in the Hirabayashi GSJ borehole. In P. K. Harvey et al. (Eds.), *Petrophysical properties of crystalline rocks* (Vol. 240, pp. 61–74, Special Publications). London, UK: Geological Society. https://doi.org/10.1144/GSL.SP.2005.240.01.06

Janku-Capova, L., Sutherland, R., Townend, J., Doan, M., Massiot, C., Coussens, J., et al. (2018). Fluid flux in fractured rock of the Alpine Fault hanging-wall determined from temperature logs in the DFDP-2B borehole, New Zealand. *Geochemistry, Geophysics, Geosystems*. https://doi.org/10.1029/2017GC007317

Jeppson, T. N., & Tobin, H. J. (2015). San Andreas fault zone velocity structure at SAFOD at core, log, and seismic scales. *Journal of Geophysical Research: Solid Earth*, *120*, 4983/4997. https://doi.org/10.1002/2015JB012043

Li, H., Wang, H., Xu, Z., Si, J., Pei, J., Li, T., et al. (2013). Characteristics of the fault-related rocks, fault zones and the principal slip zone in the Wenchuan Earthquake Fault Scientific Drilling Project Hole-1 (WFSD-1). *Tectonophysics*, *584*, 23–42. https://doi.org/10.1016/j.tecto.2012.08.021

Li, H., Xu, Z., Niu, Y., Kong, G., Huang, Y., Wang, H., et al. (2014). Structural and physical property characterization in the Wenchuan earthquake Fault Scientific Drilling project-hole 1 (WFSD-1). *Tectonophysics*, *619–620*, 86–100. https://doi.org/10.1016/j.tecto.2013.08.022

Lin, A., Maruyama, T., & Kobayashi, K. (2007). Tectonic implications of damage zone-related fault-fracture networks revealed in drill core through the Nojima fault, Japan. *Tectonophysics*, *443*(3–4), 161–173. https://doi.org/10.1016/j.tecto.2007.01.011

Lin, W., Conin, M., Moore, J. C., Chester, F. M., Nakamura, Y., Mori, J. J., et al. (2013). Stress state in the largest displacement area of the 2011 Tohoku-Oki Earthquake. *Science*, *339*(6120), 687–690. https://doi.org/10.1126/science.1229379

Little, T. A., Cox, S., Vry, J. K., & Batt, G. (2005). Variations in exhumation level and uplift rate along the oblique-slip Alpine fault, central Southern Alps, New Zealand. *Geological Society of America Bulletin*, *117*(5), 707–723. https://doi.org/10.1130/B25500.1

Little, T. A., Holcombe, R., & Ilg, B. (2002). Ductile fabrics in the zone of active oblique convergence near the Alpine Fault, New Zealand: Identifying the neotectonic overprint. *Journal of Structural Geology*, *24*(1), 193–217. https://doi.org/10.1016/s0191-8141(01)00059-1

Little, T. A., Prior, D. J., & Toy, V. G. (2016). Are quartz LPOs predictably oriented with respect to the shear zone boundary?: A test from the Alpine Fault mylonites, New Zealand. *Geochemistry, Geophysics, Geosystems*, *17*, 981–999. https://doi.org/10.1002/2015GC006145

Lofts, J. C., & Bourke, L. T. (1999). The recognition of artefacts from acoustic and resistivity borehole imaging devices. *Geological Society, London, Special Publications*, *159*(1), 59–76. https://doi.org/10.1144/gsl.sp.1999.159.01.03

Massiot, C., McLean, K., McNamara, D. D., Sepulveda, F., & Milicich, S. D. (2017). Discussion between a reservoir engineer and a geologist: permeability identification from completion test data and borehole image logs integration. In *Proceedings of the 39th New Zealand Geothermal Workshop*, 22–24 November, Rotorua, New Zealand.

Massiot, C., McNamara, D., & Lewis, B. (2015). Processing and analysis of high temperature geothermal acoustic borehole image logs in the Taupo Volcanic Zone, New Zealand. *Geothermics*, *53*, 190–201. https://doi.org/10.1016/j.geothermics.2014.05.010

Misra, S., Ellis, S., & Mandal, N. (2015). Fault damage zones in mechanically layered rocks: The effects of planar anisotropy. *Journal of Geophysical Research: Solid Earth*, *120*, 5432–5452. https://doi.org/10.1002/2014JB011780

Nie, X., Zou, C., Pan, L., Huang, Z., & Liu, D. (2013). Fracture analysis and determination of in-situ stress direction from resistivity and acoustic image logs and core data in the Wenchuan Earthquake Fault Scientic Drilling Borehole-2 (50–1370m). *Tectonophysics*, *593*, 161–171. https://doi.org/10.1016/j.tecto.2013.03.005

Norris, R. J., & Cooper, A. F. (1986). Small-scale fractures, glaciated surfaces, and recent strain adjacent to the Alpine fault, New Zealand. *Geology*, *14*(8), 687–690. https://doi.org/10.1130/0091-7613(1986)14<687:SFGSAR>2.0.CO;2

Norris, R. J., & Cooper, A. F. (1995). Origin of small-scale segmentation and transpressional thrusting along the Alpine fault, New Zealand. *Geological Society of America Bulletin*, *107*(2), 231–240. https://doi.org/10.1130/0016-7606(1995)107<0231:OOSSSA>2.3.CO;2.

Norris, R. J., & Cooper, A. F. (1997). Erosional control on the structural evolution of a transpressional thrust complex on the Alpine fault, New Zealand. *Journal of Structural Geology*, *19*(10), 1323–1342. https://doi.org/10.1016/s0191-8141(97)00036-9

Norris, R. J., & Cooper, A. F. (2003). Very high strains recorded in mylonites along the Alpine Fault, New Zealand: Implications for the deep structure of plate boundary faults. *Journal of Structural Geology*, *25*(12), 2141–2157. https://doi.org/10.1016/s0191-8141(03)00045-2

Norris, R. J., & Cooper, A. F. (2007). The Alpine Fault, New Zealand: Surface geology and field relationships. In T. S. D. Okaya & F. Davey (Eds.), *A continental plate boundary: Tectonics at South Island, New Zealand* (pp. 157–175). Washington, DC: American Geophysical Union. https://doi.org/10.1029/175GM09

Norris, R., Koons, P., & Cooper, A. (1990). The obliquely-convergent plate boundary in the South Island of New Zealand: Implications for ancient collision zones. *Journal of Structural Geology*, *12*(5–6), 715–725. https://doi.org/10.1016/0191-8141(90)90084-C

Paillet, F., & Kapucu, K. (1989). *Fracture characterization and fracture-permeability estimates from geophysical logs in the Mirror Lake watershed, New Hampshire* (Tech. Rep. 89–4058). Denver, CO: U.S. Geological Survey.

Pezard, P. A., & Luthi, S. M. (1988). Borehole electrical images in the basement of the Cajon Pass Scientic Drillhole, California; Fracture identification and tectonic implications. *Geophysical Research Letters*, *15*(9), 1017–1020. https://doi.org/10.1029/GL015i009p01017

Poppelreiter, M., Garcia-Carballido, C., & Kraaijveld, M. A. (2010). *AAPG Memoir 1992—Dipmeter and borehole image log technology* (1st ed.). Tulsa, OK: American Association of Petroleum Geologists.

Priest, S. D. (1993). *Discontinuity analysis for rock engineering*. Dordrecht, the Netherlands: Springer. https://doi.org/10.1007/978-94-011-1498-1

Remaud, L. (2015). *Study of the damage zone around the Alpine Fault, New-Zealand, from borehole data of the Deep Fault Drilling Project (stage 2)* (Msc). Grenoble, France: Université Joseph Fourier.

Rider, M. (1996). *The geological interpretation of well logs* (2nd ed., 280 p.). Caithness, UK: Whittles Publishing.

Schijns, H., Schmitt, D. R., Heikkinen, P. J., & Kukkonen, I. T. (2012). Seismic anisotropy in the crystalline upper crust: Observations and modelling from the Outokumpu scientific borehole, Finland. *Geophysical Journal International*, *189*(1), 541–553. https://doi.org/10.1111/j.1365-246X.2012.05358.x

Schleicher, A. M., Sutherland, R., Townend, J., Toy, V. G., & van der Pluijm, B. (2015). Clay mineral formation and fabric development in the DFDP-1B borehole, central Alpine Fault, New Zealand. *New Zealand Journal of Geology and Geophysics*, *58*(1), 13–21. https://doi.org/10.1080/00288306.2014.979841

Schmitt, D. R. (1993). Fracture statistics derived from digital ultrasonic televiewer logging. *The Journal of Canadian Petroleum Technology*, *32*(2), 34–43.

Schmitt, D. R., Currie, C. A., & Zhang, L. (2012). Crustal stress determination from boreholes and rock cores: Fundamental principles. *Tectonophysics*, *580*, 1–26. https://doi.org/10.1016/j.tecto.2012.08.029

Sibson, R. H., White, S. H., & Atkinson, B. K. (1979). Fault rock distribution and structure within the Alpine Fault Zone. A preliminary account. Bulleting of the Royal Society of New Zealand, *18*, 55–65.

Sibson, R. H., White, S. H., & Atkinson, B. K. (1981). Structure and distribution of fault rocks in the Alpine Fault Zone, New Zealand. *Geological Society, London, Special Publication*, *9*(1), 197–210. https://doi.org/10.1144/GSL.SP.1981.009.01.18

Stern, T., Okaya, D., Kleffmann, S., Scherwath, M., Henrys, S., & Davey, F. (2007). Geophysical exploration and dynamics of the Alpine Fault Zone. D. Okaya, T. Stern, & F. Davey (Eds.), In *A continental plate boundary: Tectonics at South Island, New Zealand* (pp. 207–233). Washington, DC: American Geophysical Union. https://doi.org/10.1029/175GM11

Sutherland, R., Eberhart-Phillips, D., Harris, R. A., Stern, T., Beavan, J., Ellis, S., et al. (2007). Do great earthquakes occur on the Alpine fault in central South Island, New Zealand?. In D. Okaya, T. Stern, & F. Davey (Eds.), *A continental plate boundary: Tectonics at South Island, New Zealand* (pp. 235–251). Washington, DC: American Geophysical Union. https://doi.org/10.1029/175GM12

Sutherland, R., Townend, J., Toy, V. G., Allen, M., Baratin, L., Barth, N., et al. (2015). *Deep Fault Drilling Project (DFDP), Alpine Fault. Boreholes DFDP-2A and DFDP-2B technical completion report* (Tech. Rep. 2015/50). Lower Hutt, NZ: GNS Science.

Sutherland, R., Townend, J., Toy, V. G., Upton, P., Coussens, J., Allen, M., et al. (2017). Extreme hydrothermal conditions at an active plate-bounding fault. *Nature*, *546*(7656), 137–140. https://doi.org/10.1038/nature22355

Sutherland, R., Toy, V. G., Townend, J, Cox, S. C., Eccles, J. D., Faulkner, D. R., et al. (2012). Drilling reveals fluid control on architecture and rupture of the Alpine fault, New Zealand. *Geology*, *40*(12), 1143–1146. https://doi.org/10.1130/g33614.1

Terzaghi, R. D. (1965). Sources of error in joint surveys. *Geotechnique*, *15*(3), 287–304. https://doi.org/10.1680/geot.1965.15.3.287

Townend, J., Sutherland, R., & Toy, V. (2009). Deep Fault Drilling Project—Alpine Fault, New Zealand. *Scientific Drilling*, *8*, 75–82. https://doi.org/10.2204/iodp.sd.8.12.2009

Townend, J., Sutherland, R., Toy, V. G., Doan, M.-L., Celerier, B., Massiot, C., et al. (2017). Petrophysical, geochemical, and hydrologic evidence for extensive fracture-mediated fluid and heat transport in the Alpine Fault's hanging-wall damage zone. *Geochemistry, Geophysics, Geosystems*, *18*, 4709–4732. https://doi.org/10.1002/2017GC007202

Townend, J., Sutherland, R., Toy, V. G., Eccles, J. D., Boulton, C., Cox, S. C., et al. (2013). Late-interseismic state of a continental plate-bounding fault: Petrophysical results from DFDP-1 wireline logging and core analysis, Alpine Fault, New Zealand. *Geochemistry, Geophysics, Geosystems*, *14*, 3801–3820. https://doi.org/10.1002/ggge.20236

Townend, J., & Zoback, M. D. (2000). How faulting keeps the crust strong. *Geology*, *28*(5), 399–402. https://doi.org/10.1130/0091-7613(2000)28<399:HFKTCS>2.0.CO

Toy, V. G., Boulton, C. J., Sutherland, R., Townend, J., Norris, R. J., Little, T. A., et al. (2015). Fault rock lithologies and architecture of the central Alpine fault, New Zealand, revealed by DFDP-1 drilling. *Lithosphere*, *7*(2), 155–173. https://doi.org/10.1130/l395.1

Toy, V. G., Norris, R., Prior, D., Walrond, M., & Cooper, A. (2013). How do lineations reflect the strain history of transpressive shear zones? The example of the active Alpine Fault zone, New Zealand. *Journal of Structural Geology*, *50*, 187–198. https://doi.org/10.1016/j.jsg.2012.06.006

Toy, V. G., Prior, D. J., Norris, R. J., Cooper, A. F., & Walrond, M. (2012). Relationships between kinematic indicators and strain during syn-deformational exhumation of an oblique slip, transpressive, plate boundary shear zone: The Alpine Fault, New Zealand. *Earth and Planetary Science Letters*, *333–334*, 282–292. https://doi.org/10.1016/j.epsl.2012.04.037

Toy, V. G., Ritchie, S., & Sibson, R. H. (2011). Diverse habitats of pseudotachylytes in the Alpine Fault Zone and relationships to current seismicity. *Geological Society, London, Special Publications*, *359*(1), 115–133. https://doi.org/10.1144/SP359.7

Toy, V. G., Sutherland, R., Townend, J., Allen, M. J., Becroft, L., Boles, A., et al. (2017). Bedrock geology of 1 DFDP-2B, Central Alpine Fault, New Zealand. *New Zealand Journal of Geology and Geophysics*, *60*(4), 497–518.

Upton, P., Song, B. R., & Koons, P. O. (2018). Topographic control on shallow fault structure and strain partitioning near Whataroa, New Zealand demonstrates weak Alpine Fault. *New Zealand Journal of Geology and Geophysics*, *61*(1), 1–8. https://doi.org/10.1080/00288306.2017.1397706

Wagner, W., & Kretzschmar, H. (2007). *International Steam Tables—Properties of Water and Steam based on the Industrial Formulation IAPWS-IF97* (2nd ed., 350 p.). Berlin, Germany: Springer. https://doi.org/10.1007/978-3-540-74234-0

Wenning, Q. C., Berthet, T., Ask, M., Zappone, A., Rosberg, J. E., & Almqvist, B. S. G. (2017). Image log analysis of in situ stress orientation, breakout growth, and natural geologic structures to 2.5 km depth in central Scandinavian Caledonides: Results from the COSC-1 borehole. *Journal of Geophysical Research: Solid Earth*, *122*, 3999–4019. https://doi.org/10.1002/2016JB013776

Wightman, R. H., & Little, T. A. (2007). Deformation of the Pacific Plate above the Alpine fault ramp and its relationship to expulsion of metamorphic fluids: An array of backshears. In D. Okaya, T. Stern, & F. Davey (Eds.), *A continental plate boundary: Tectonics at South Island, New Zealand* (pp. 177–205). Washington, DC: American Geophysical Union. https://doi.org/10.1029/175GM10

Williams, J. H., & Johnson, C. D. (2004). Acoustic and optical borehole-wall imaging for fractured-rock aquifer studies. *Journal of Applied Geophysics*, *55*(1–2), 151–159. https://doi.org/10.1016/j.jappgeo.2003.06.009

Williams, J. N. (2017). *The damage zone of New Zealand's Alpine Fault* (PhD thesis, 229 p.). Dunedin, New Zealand: University of Otago. https://otago.ourarchive.ac.nz/handle/10523/7360.

Williams, J. N., Toy, V. G., Massiot, C., McNamara, D. D., Smith, S. A. F., & Mills, S. (2018). Controls on fault zone structure and brittle fracturing in the foliated hanging-wall of the Alpine Fault. *Solid Earth*, *9*, 469–489. https://doi.org/10.5194/se-9-469-2018

Williams, J. N., Toy, V. G., Massiot, C., McNamara, D. D., & Wang, T. (2016). Damaged beyond repair? Characterising the damage zone of a fault late in its interseismic cycle, the Alpine Fault, New Zealand. *Journal of Structural Geology*, *90*, 76–94. https://doi.org/10.1016/j.jsg.2016.07.006

Williams, J. N., Toy, V. G., Smith, S. A. F., & Boulton, C. (2017). Fracturing, fluid-rock interaction and mineralisation during the seismic cycle along the Alpine Fault. *Journal of Structural Geology*, *103*, 151–166. https://doi.org/10.1016/j.jsg.2017.09.011

Yow, J. (1987). Blind zones in the acquisition of discontinuity orientation data. *International Journal of Rock Mechanics and Mining Sciences & Geomechanics Abstracts*, *24*(5), 317–318. https://doi.org/10.1016/0148-9062(87)90868-0

Zemanek, J., Glenn, E. E., Norton, L. J., & Caldwell, R. L. (1970). Formation evaluation by inspection with the borehole televiewer. *Geophysics*, *35*(2), 254–269. https://doi.org/10.1190/1.1440089

Zoback, M., Barton, C., Brudy, M., Castillo, D., Finkbeiner, T., Grollimund, B., et al. (2003). Determination of stress orientation and magnitude in deep wells. *International Journal of Rock Mechanics and Mining Sciences*, *40* (7–8), 1049–1076. https://doi.org/10.1016/j.ijrmms.2003.07.001

Zoback, M., Hickman, S., & Ellsworth, W. (2007). The role of fault zone drilling. In G. Schubert (Ed.), *Treatise on geophysics* (pp. 649–674). Amsterdam, the Netherlands: Elsevier. https://doi.org/10.1016/b978-044452748-6.00084-5

Zoback, M. D., & Townend, J. (2001). Implications of hydrostatic pore pressures and high crustal strength for the deformation of intraplate lithosphere. *Tectonophysics*, *336*(1–4), 19–30. https://doi.org/10.1016/S0040-1951(01)00091-9